



# Aerosol Deposition of $\text{CuFeO}_2$ Photocathode Coatings for Hydrogen Production

Alessia Bruera<sup>1,2</sup> · Andreas Elsenberg<sup>3</sup> · Mauro Borghi<sup>4</sup> · Giulia Dolcetti<sup>1</sup> · Giovanni Bolelli<sup>1,2,5</sup> · Frank Gärtner<sup>3</sup> · Mauricio Schieda<sup>6</sup> · Thomas Klassen<sup>3,6</sup> · Luca Lusvarghi<sup>1,2,5</sup>

Submitted: 5 March 2024 / in revised form: 30 May 2024 / Accepted: 11 June 2024  
© The Author(s) 2024

**Abstract** Photoelectrochemical (PEC) water splitting is a viable route for green hydrogen generation. In PEC cells, the electrodes are coated with suitable semiconductor materials, which absorb the sunlight, generating charge carriers that are used to split water molecules into  $\text{H}_2$  and  $\text{O}_2$ .  $\text{CuFeO}_2$  is one promising photocathode material for water splitting. However, its performance is limited by electron/hole pairs recombination within the film and at the film/substrate interface. Aerosol deposition (AD) can be employed to minimize charge recombination by spraying dense, thin films and by establishing a good back-contact interface. In this study,  $\text{CuFeO}_2$  powders were synthesized through a conventional solid-state technique and sprayed by AD under varied parameter sets. The effect of particle size distributions, carrier gas, gas pressure and substrate temperature was investigated. The best spraying parameter set was then tuned to obtain thin coatings ( $< 1 \mu\text{m}$ ). Single-

particle deformation and coatings microstructure were investigated by scanning electron microscopy. Optical properties of  $\text{CuFeO}_2$  films were analyzed by UV–Vis spectroscopy, while photoelectrochemical performances were estimated through amperometry tests under simulated sunlight. The results of this research show that  $\text{CuFeO}_2$  photocathodes can be successfully manufactured by AD. Their performance can be optimized by adjusting coating thickness and by annealing in air.

**Keywords** aerosol deposition ·  $\text{CuFeO}_2$  · hydrogen generation · photocathode coatings · sunlight harvesting

## Introduction

As a renewable energy carrier, hydrogen can play a major role in the development of a climate neutral economy.  $\text{H}_2$  is extremely versatile, being suitable for producing synthetic fuels (ammonia, methane, methanol) (Ref 1, 2), steels (Ref 3) and for generating clean electrical energy in fuel cells (Ref 4). Hydrogen can also be used to efficiently store energy over long periods of time in different forms: in the gaseous state in high-pressure tanks, as a liquid in cryogenic tanks, and in solid-state systems (Ref 5-7). Nowadays, hydrogen is mainly produced out of fossil fuels by gas steam reforming. This method is fast, cheap and efficient, but it generates greenhouse gases (Ref 8-10). In order to ensure an efficient contribution to the energy transition process, hydrogen should be only generated from renewable resources, as ‘green’ hydrogen (Ref 11). This is fundamental to prevent the depletion of natural resources and the emission of  $\text{CO}$ ,  $\text{CO}_2$ ,  $\text{SO}_2$  and  $\text{NO}_x$ . In addition, the use of green hydrogen can stabilize and balance the distribution of renewable resources: during overproduction or

✉ Alessia Bruera  
alessia.bruera@unimore.it

<sup>1</sup> Department of Engineering “Enzo Ferrari”, University of Modena and Reggio Emilia, Via Pietro Vivarelli 10, 41125 Modena, Italy  
<sup>2</sup> INSTM Research Unit, University of Modena and Reggio Emilia, Via Pietro Vivarelli 10, 41125 Modena, Italy  
<sup>3</sup> Helmut Schmidt University, University of the Federal Armed Forces Hamburg, Holstenhofweg 85, 22043 Hamburg, Germany  
<sup>4</sup> Institute for Microelectronics (TU Wien), Gusshausstrasse 27–29, 1040 Vienna, Austria  
<sup>5</sup> InterMech–MO.RE., University of Modena and Reggio Emilia, Via Pietro Vivarelli 2, 41125 Modena, Italy  
<sup>6</sup> Helmholtz-Zentrum Hereon GmbH, 21502 Geesthacht, Germany

low-demand periods, the surplus of renewable energies can be efficiently stored as  $H_2$  for later usage or grid distribution (Ref 12). This is particularly important for expanding the field of solar energy, which is an inexhaustible source of energy, but strongly limited by time and weather conditions (Ref 13).

Photoelectrochemical (PEC) water splitting is one of the most promising technologies for green hydrogen generation powered by sunlight. The PEC process represents a valid alternative to the traditional photovoltaic systems, which usually require external electrolyzers and several electron transfer steps (Ref 13, 14). In PEC cells, the electrodes are usually made of or coated with suitable semiconductor materials (p-type for photocathodes and n-type for photoanodes) which harvest the sunlight and generate charge carriers that drive the water splitting reaction (Ref 15). Figure 1 schematically shows the basic principles of a PEC cell when a single-absorber photocathode is employed. (i) The p-type semiconductor electrode absorbs photons with energies equal or greater than the energy band gap ( $E_g$ ), and (ii) some of the valence band electrons ( $e^-$ ) are promoted into the conduction band, creating holes ( $h^+$ ). (iii) The photogenerated electron/hole pairs separate and travel through the semiconductor. (iv) While the electrons are employed in the reduction of water (hydrogen evolution reaction—HER) on the photocathode/electrolyte interface, the holes participate in the oxidation reaction (oxygen evolution reaction—OER) at the anodic interface to the substrate (Ref 12–14, 16–18). Thus, the photoelectrode material should be able to absorb significant quantities of the sunlight and produce a sufficiently high voltage for efficient water splitting (Ref 19).

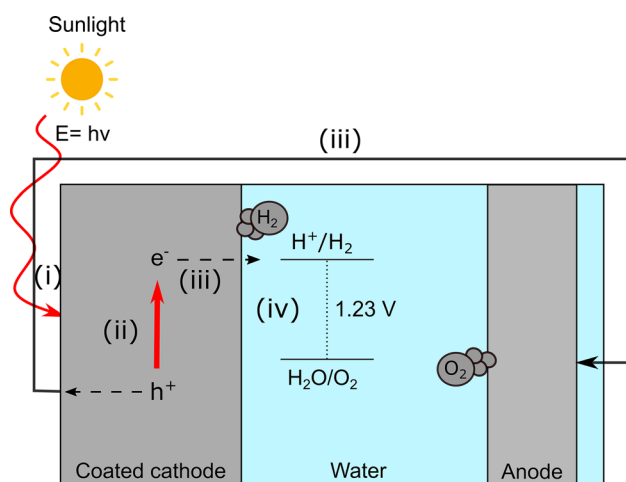


**Fig. 1** Schematic illustration of the basic principles of the photoelectrochemical (PEC) water splitting process for a photocathode material. (i) The cathode absorbs the sunlight and (ii) generates electron/hole pairs. (iii) The charge carriers are separated and transported to the electrodes' surfaces to (iv) split water into hydrogen and oxygen

While n-type materials have been widely investigated and optimized (Ref 20–25), only little progress has been made for the development of stable p-type electrodes (Ref 26, 27). One promising candidate—made of non-toxic, earth-abundant elements—is the delafossite  $CuFeO_2$  (Ref 28). This material has a suitable band position for HER and a band gap energy of  $\approx 1.5$  eV, resulting in the absorption of the visible light ( $\lambda = 380\text{--}700$  nm), which represent 48% of the total solar spectrum (Ref 29, 30). According to these features,  $CuFeO_2$  photocathodes should be able to generate photocurrents of up to  $10\text{--}15$  mA/cm<sup>2</sup> (Ref 31). However, so far, bare  $CuFeO_2$  coatings exhibited poor current densities. PEC performances can be enhanced (up to  $2.4$  mA/cm<sup>2</sup> at  $0.4$  V<sub>RHE</sub>) by performing post-deposition treatments and by using catalysts or heterojunctions (Ref 32, 33). Despite the post-treatments, these values are still 4–7 times lower than expected from theory. The discrepancy between theoretical and experimental photocurrent density is mainly attributed to short electron diffusion lengths and recombination of photogenerated electron/hole pairs within the film and the film/substrate interface (Ref 34, 35).

Energy losses may be minimized by using aerosol deposition (AD) to form dense films in sub-micrometer thickness and by establishing a good back-contact interface. The feasibility of manufacturing photoelectrodes by AD has already been demonstrated for  $BiVO_4$  (Ref 24, 36). AD is a solid-state kinetic spraying method used to deposit dense ceramic coatings at room temperature on a wide range of substrate materials. It offers several advantages compared to conventional coating techniques. By operating at room temperature, oxidation and other undesired reactions can be avoided during spraying, leading to the formation of high-purity coatings, with the same composition of the feedstock material and refined crystal structures. Indeed, AD films exhibit high-density and nanocrystalline structures, which usually result in good mechanical, thermal and electrical properties. Furthermore, a wide range of coating thicknesses (from few hundreds of nanometers to 1 mm) can be obtained with AD by adjusting the spraying parameters or the number of scans. Another advantage is the possibility to deposit high-quality coatings in a short time: while conventional film growth techniques have deposition rates between  $0.01$  and  $0.05$   $\mu\text{m}/\text{min}$ , AD exhibits film growth rates of  $5\text{--}50$   $\mu\text{m}/\text{min}$  (Ref 37, 38). In the AD process, dried fine powders ( $200$  nm– $2$   $\mu\text{m}$ ) are dispersed in a carrier gas stream to form the aerosol, which is then accelerated through a converging or converging–diverging nozzle into the deposition chamber. The difference between process gas pressure within the nozzle and the deposition chamber (usually operating in low vacuum) causes expansion and further acceleration of the gas stream of up to several hundreds of m/s. When the particles impact

on the substrate surface, the attained kinetic energy is converted into deformation and particle fracture, leading to particle–particle and particle–substrate bonding (Ref 38–40). The specific mechanisms of bonding and energy conversion are still under discussion (Ref 41, 42). However, successful bonding in aerosol deposition is typically associated with a grain refinement of the original powder microstructure by more than one order of magnitude. This phenomenon is attributed to internal deformation and fracture occurring upon particle impact rather than local heat concentration and melting, as reported in several experimental works (Ref 38, 40, 41, 43, 44). Taking  $\text{CeO}_2$  as an example, Exner et al. (Ref 44) even derived a minimum initial grain size needed for later grain refinement and successful coating build-up during AD, noting that grain refinement was also associated with an increase in microstrain. By applying a molecular dynamics simulation to model the particle impact in AD, Daneshian et al. (Ref 45) studied the effect of local heating during AD. Their results showed that, upon impact, the local material deformation in shear band-like features causes local heating to temperatures of up to 500 °C. Locally reached higher temperatures might support activation of secondary slip systems for deformation. However, within this small dimension, the heat dissipates over the particle volume in less than a nanosecond, leading to only a minor overall temperature rise. Thus, the absolute temperatures of 500 °C and the short time spans for temperature exposure are not sufficient for activating recrystallization, confirming that the observed grain refinement in AD can be mainly attributed to deformation and fracture.

So far, only Stocker et al. (Ref 46) deposited  $\text{CuFeO}_2$  powders by AD, mainly studying the effect of oxygen partial pressure on the thermoelectric properties of coatings. However, systematic studies to derive effects of the main AD process parameters for  $\text{CuFeO}_2$  are still missing. Respectively, the first part of the present study investigates the effect of (i) particle size distribution, (ii) process gas type, (iii) gas flow/pressure and (iv) substrate temperature on layer build-up as well as attained  $\text{CuFeO}_2$  microstructures. In the second part, the most promising spraying parameters were tuned to obtain thin coatings ( $< 1 \mu\text{m}$ ) on fluorine-doped tin oxide (FTO)-glass substrates in order to investigate respective photoelectrochemical performances.

## Materials and Methods

### Material Preparation

Copper iron oxide ( $\text{CuFeO}_2$ ) powders have been synthesized through a conventional mixed-oxide method, as reported in the literature (Ref 46). Iron(III) oxide (98%,

Alfa Aesar, Karlsruhe, Germany) and copper(I) oxide (97%, Alfa Aesar, Karlsruhe, Germany) were employed as powder precursors. Stoichiometric ratios of the raw precursor powders were mixed and processed in a planetary ball mill (Retsch PM 100 model, Verder Scientific, Haan, Germany) using a zirconia grinding vial, 5-mm zirconia grinding balls and ethanol as solvent. The weight ratio of milling balls, powder and ethanol was set to 10 : 1 : 0.2. Milling was conducted at 300 rpm for 4 hours with breaks of 5 minutes every 10 minutes of milling for cooling. After milling, solvent residuals were evaporated under the fume hood. The reaction of the mixed oxides was then performed in a tube furnace (model RS 80/500/13, Nabertherm GmbH, Lilienthal, Germany) at 1100 °C for 12 hours under constant argon flux (200 l/h). The heating rate was fixed at 350 °C/h, while a water-based refrigeration system was employed in order to avoid overheating and for ensuring defined cooling of the chamber. The synthesized  $\text{CuFeO}_2$  powders were then pre-milled for 60 s using 10-mm zirconia balls by applying a Pulverisette 5/4 planetary mill (Fritsch GmbH, Idar-Oberstein, Germany). Subsequently, powders were reground at 400 rpm with 2-mm zirconia balls and isopropanol as solvent. The weight ratio of milling balls, powder and isopropanol was fixed to 10 : 1 : 0.5. Three different particle size distributions were obtained by setting the milling times to 90 s, 8 min and 60 min, respectively, with 10-min breaks for cooling after 1 min of milling. The powders were then dried in vacuum ( $\approx 10^{-2}$  MPa) at 250 °C for 8 h, cooled down and stored in a glove box.

Stainless steel AISI 304 plates, with a lateral size of 10 mm × 10 mm and 3 mm in thickness, were used as substrates for coating deposition during parameter development and single-impact tests. The plates were polished until reaching a maximum surface roughness of  $R_a = 1 \mu\text{m}$ . The thin coatings for photoelectrochemical analyses were deposited on FTO-glass plates (dimensions of 15 mm × 30 mm and 2 mm thickness), provided by Solaronix SA, Aubonne, Switzerland. Both types of substrates were cleaned in ultrasonic bath by using first distilled water and then ethanol for 15 min each. In addition, directly before spraying, the substrates were plasma etched in oxygen atmosphere at 0.3 bar for 5 min to remove possible adsorbates (PICO machine, Diener Plasma GmbH&Co KG, Ebenhausen, Germany).

### Powder Morphology and Particles Size Analysis

The morphology of the  $\text{Cu}_2\text{O}$ ,  $\text{Fe}_2\text{O}_3$  and the as-synthesized  $\text{CuFeO}_2$  powders was investigated by using Scanning Electron Microscope (ESEM: Quanta 200, from FEI—Thermo Fischer Scientific, Eindhoven, NL) equipped with EDX detector. The mean particle size of  $\text{Cu}_2\text{O}$  and  $\text{Fe}_2\text{O}_3$

was estimated by image analysis (ImageJ: NIH, Bethesda, USA) on the SEM micrographs, while the particle size distributions of the milled CuFeO<sub>2</sub> powders were analyzed by laser scattering (LA-910 from Horiba, Kyoto, Japan).

### Aerosol Deposition

CuFeO<sub>2</sub> coatings were deposited by using a laboratory-built aerosol deposition system, a De Laval slit nozzle with nozzle throat dimensions of 4.0 mm × 0.2 mm and a RBG 1000ISD from Palas GmbH, Karlsruhe, Germany, as powder feeder. The different conditions used for parameter development are summarized in Table 1. The effect of different particle size distributions, carrier gas, gas flow/pressure and substrate temperature was studied. For selected sets of experiments, the substrate temperature was increased up to 400 °C by using a titanium high-temperature resistance heater PZ28-3 T from Harry Gestigkeit GmbH, Düsseldorf, Germany. The substrates were fixed to the heating plate and the whole setup being attached to the robotic system to apply the defined motion for building-up layers during the spraying process, by staying at defined temperatures. The samples were then cooled down by flooding the deposition chamber with air. One-, two- and four-layer coatings were deposited with the same set of parameters. In order to deposit single particles, the traverse line speed of the sample holder and the powder feeding rate were adjusted according to the powder sizes: A traverse speed of 5, 15 and 25 mm/s was employed for batch 1 ( $D_{50} = 2.2 \mu\text{m}$ ), batch 2 ( $D_{50} = 1 \mu\text{m}$ ) and batch 3 ( $D_{50} = 0.6 \mu\text{m}$ ), respectively, and feeding rates of 0.4 cm<sup>3</sup>/h for batch 1 and 2 and 0.2 cm<sup>3</sup>/h for batch 3 were employed. The deposition of thin CuFeO<sub>2</sub> coatings on FTO-glass substrates was carried out by using the parameter sets given in Table 2. In order to reduce the coating thickness, three strategies were employed: (i) decreasing

the feeding rate from 3.8 cm<sup>3</sup>/h to 1.9 or 1 cm<sup>3</sup>/h or (ii) by adding two types of cyclones (Z1000 and Z500 from Palas GmbH, Karlsruhe, Germany), in sequence, into the process gas line and (iii) increasing of the traverse speed. As sort of aerodynamic filters, the cyclones cutoff coarser particles and possible agglomerates (larger than 10 μm and 5 μm, respectively, for Z1000 and Z500) and generally reduce the number of spraying particles. Sets of optimized thin CuFeO<sub>2</sub> films were annealed in air at 550 °C in a muffle furnace for 1 h.

It should be noted that both gas flow (which indicates the gas consumption) and gas pressure are indicated in the tables and in the following figures. For consistency, the results will be mainly discussed in terms of gas pressures.

### Analyses of Phase Composition and Characterization of Coating Microstructures

The phase composition of as-synthesized CuFeO<sub>2</sub> powder and as-sprayed coatings was assessed by X-ray diffraction (XRD: X'Pert PRO, PANalytical, Almelo, the Netherlands) using Cu-Kα radiation (wavelength: 1.540598 nm) and the X'Celerator detector. The diffraction patterns were collected over a range of 20°–80° by applying a step size of 0.02°. Chemical analyses were performed with the EDX detector of the ESEM (INCA, from Oxford Instruments Analytical, Abingdon, UK). The morphology of the single-impact tests and the coatings' microstructure were analyzed by high-resolution scanning electron microscopy (HR-SEM) using a dual-beam Helios G4 UC from FEI, now Thermo Fisher Scientific Inc., Waltham, Massachusetts, USA, equipped with a focused ion beam (FIB) of Ga<sup>+</sup> ions. The acceleration voltage was adjusted to 10 kV. The single-impact morphologies (wipe tests) were examined under perspective view (samples tilted by 52°) in order to properly evaluate particle bonding and

**Table 1** Conditions during development of parameter sets for aerosol deposition of CuFeO<sub>2</sub> by using stainless steel (AISI 304) substrates

Parameters	Values
Powders	Batch 1: $D_{50} = 2.2 \mu\text{m}$ Batch 2: $D_{50} = 1 \mu\text{m}$ Batch 3: $D_{50} = 0.6 \mu\text{m}$
Process gases	Nitrogen, Helium
Pressures in the aerosol generation unit Gas flows	$0.9 \times 10^{-1}$ , $1.6 \times 10^{-1}$ , $2.9 \times 10^{-1}$ MPa 10, 20, 40 L/min
Pressures in the deposition chamber	$2 \times 10^{-5}$ , $5 \times 10^{-5}$ , $1 \times 10^{-4}$ MPa
Traverse line speeds of the sample holder	Coating: 5 mm/s Single impact test: 5, 15, 25 mm/s
Aerosol feeding rates	Coating: 3.8 cm <sup>3</sup> /h Single impact test: 0.2, 0.4 cm <sup>3</sup> /h
Spray distances	25 mm
Substrate temperatures	25, 100, 200, 400 °C

**Table 2** Spraying parameters for the aerosol deposition of thin functional CuFeO<sub>2</sub> films for photo electrochemical analyses on FTO-glass substrates

Parameters	Values
Powders	Batch 2: $D_{50} = 1 \mu\text{m}$ Batch 3: $D_{50} = 0.6 \mu\text{m}$
Process gases	Nitrogen, Helium
Pressure in the aerosol generation unit	$2.9 \times 10^{-1} \text{ MPa}$
Gas flow	40 L/min
Pressure in the deposition chamber	$1 \times 10^{-4} \text{ MPa}$
Traverse line speeds of the sample holder	10, 15, 20, 25 mm/s
Aerosol feeding rates	1, 2, 3.8 cm <sup>3</sup> /h
Filters	Cyclone Z1000, Z5000
Spray distance	25 mm

deformation. Coating cross sections were prepared in situ in the HR-SEM by FIB cutting or alternatively by means of metallographic preparation. In the former case, two thin layers of Pt were deposited to achieve sample conductivity for SEM imaging and for coating protection before FIB cutting. Additional observations were carried out on cross sections prepared by conventional metallographic procedures. These included cutting of the coated samples with a resin-bound Al<sub>2</sub>O<sub>3</sub>-based abrasive disc in a Micromet machine (Remet, Casalecchio di Reno, Italy), embedding in epoxy resin, grinding with SiC-based abrasive papers and polishing down to a QUOTE 60-nm colloidal silica suspension on a nap cloth by using a LaboPol-5 polishing machine (Struers, Denmark).

### Analyses of Functional Properties

The optical properties of the coatings were studied by measuring the transmittance and reflectance spectra with a UV-Vis-NIR spectrophotometer (Cary 5000, Agilent).

Photoelectrochemical (PEC) characterizations were performed in a three-electrode cell (PECC2, Zahner-Elektrik GmbH, Kronach, Germany) controlled by an electrochemical workstation (Zennium, Zahner-Elektrik). The samples were connected as working electrode (WE), while a Pt wire was used as counter electrode (CE). The reference electrode (RE) used was Hg/HgO (RE-61AP, ALS, Japan vs SHE), due to its stability in alkaline media. The tests were conducted in 1 M NaOH solution (pH  $\approx$  14), purged with argon or oxygen for at least 15 minutes prior to the test. The samples were illuminated through a quartz window using a solar simulator (Class AAA, AM1.5G, 1000 W/m<sup>2</sup>; LOT Quantum Design, Darmstadt, Germany). The exposed area of the samples was defined by a 5-mm O-ring, roughly corresponding to a nominal area of  $\approx$  0.196 cm<sup>2</sup>. After assembling and connecting the cell, the samples were left in contact with the electrolyte solution for 5 minutes in the dark, to reach the open-circuit potential (OCP). The photoresponse and the stability of the samples were then

studied by performing chrono-amperometry tests under chopped light illumination, obtained by opening and closing a shutter between the light source and the cell at a frequency of 200 mHz. A constant potential of  $-0.5 \text{ V}$  vs Hg/HgO reference electrode was applied for 10 minutes, corresponding to  $+0.44 \text{ V}$  vs RHE (reversible hydrogen electrode) as calculated from the Nernst equation:

$$E_{(RHE)} = E_{(Hg/HgO)} + E_{(Hg/HgO)}^0 + 0.059 \times pH$$

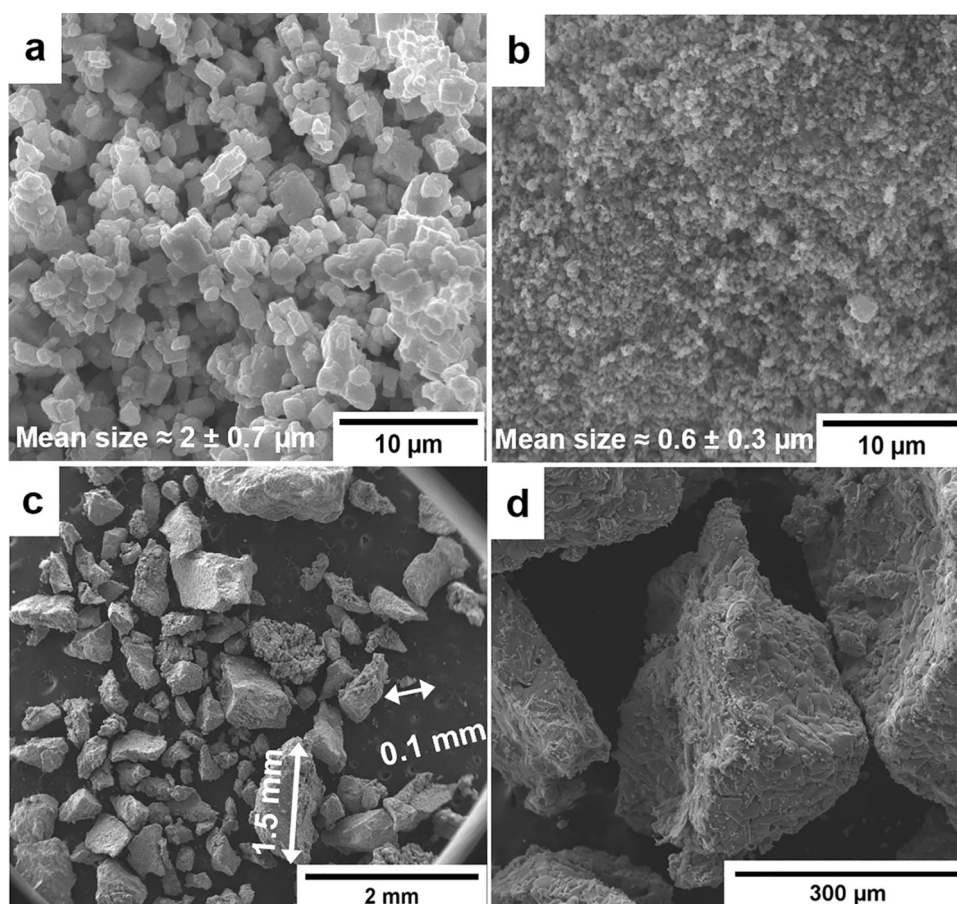
During chrono-amperometry tests, the current ( $i$ ) was measured vs time. Current densities ( $j$ ) were then obtained by dividing the measured currents (in  $\mu\text{A}$ ) by the nominal exposed area (0.196 cm<sup>2</sup>). The difference in magnitude between the current densities in the dark and under illumination is defined as photocurrent density ( $\mu\text{A}/\text{cm}^2$ ), and it is proportional to the rate of hydrogen generation.

## Results

### Powder Morphologies and Sizes

CuFeO<sub>2</sub> powders were synthesized through a solid-state reaction between Cu<sub>2</sub>O and Fe<sub>2</sub>O<sub>3</sub>. By observing the SEM micrographs of powders in Fig. 2, it can be noted that the powder synthesis process causes particle agglomeration by partial sintering. While the powder precursors (Fig. 2a,b) are rather fine—having an average particle size of  $2 \mu\text{m} \pm 0.7 \mu\text{m}$  for Cu<sub>2</sub>O and  $0.6 \mu\text{m} \pm 0.3 \mu\text{m}$  for Fe<sub>2</sub>O<sub>3</sub>—as-synthesized CuFeO<sub>2</sub> powders consist of loosely bonded sintered bodies with angular morphologies (Fig. 2c,d). The cluster dimension ranges from 0.1 mm to 1.5 mm. In order to ensure defined conditions for further procedures, a pre-milling step was conducted to break and crush the main agglomerates. The powders were then milled for different times to adjust the particle sizes, as described in section “[Material preparation](#).” The morphologies and the particle size distributions of the milled CuFeO<sub>2</sub> powders are shown in Fig. 3. Irrespective of process time, all milled powders

**Fig. 2** Powder morphologies as SEM micrographs (SE mode) of the powder precursors (a)  $\text{Cu}_2\text{O}$  and (b)  $\text{Fe}_2\text{O}_3$ , and (c,d) the as-synthesized  $\text{CuFeO}_2$  powders supplying an overview and details, respectively



have angular, fractured morphologies and rather smooth surfaces (Fig. 3a,b,c). By milling, the particle sizes are drastically reduced, but the finer particles still tend to aggregate around the coarser ones. Nevertheless, all milled powder batches exhibit a narrow particle size distribution, as shown in Fig. 3(d). Short milling times (90 s) are already sufficient to obtain a particle size distribution of  $D_{10} = 0.5 \mu\text{m}$ ,  $D_{50} = 2.2 \mu\text{m}$  and  $D_{90} = 5.5 \mu\text{m}$ . Increasing the milling time from 90 s to 8 min mainly affects the  $D_{50}$  and  $D_{90}$  values, both decreasing by a factor of 2.2. Longer processing times (60 min) only result in the decrease of the average particle size ( $D_{50}$ ) by a factor of 1.7, while the  $D_{10}$  and  $D_{90}$  values are comparable. It should be noted here that the  $D_{10}$  values are probably slightly overestimated by laser diffraction analysis since they are close to the lower detection limit of the technique. SEM micrographs at higher magnification reveal that few smaller particles ( $\approx 0.1 \mu\text{m}$ ) are formed after 60 min of milling. According to pre-requisites reported in the literature, all powder batches have suitable morphology and dimensions for aerosol deposition (Ref 40, 41).

### Powder and Coating Composition and Crystal Structure

The formation of  $\text{CuFeO}_2$  delafossite phase after the solid-state reaction in argon at  $1100 \text{ }^\circ\text{C}$  was confirmed by x-ray diffraction analysis. Moreover, as expected for aerosol-deposited coatings, the  $\text{CuFeO}_2$  phase is retained after the deposition for all substrates temperatures, too low to induce further oxidation or any other change in the phase composition during spraying. The diffraction pattern of synthesized and milled powder (black) and respective coatings sprayed with helium as process gas at  $2.9 \times 10^{-1} \text{ MPa}$  on room temperature ( $25 \text{ }^\circ\text{C}$ , red line) or heated substrates ( $100 \text{ }^\circ\text{C}$ , blue line;  $200 \text{ }^\circ\text{C}$ , pink line;  $400 \text{ }^\circ\text{C}$ , green line) are compared in Fig. 4. All the patterns exhibit the characteristic diffraction peaks of  $\text{CuFeO}_2$  (indicated by \*), in good agreement to the reference pattern JCPDS n° 00-39-0246. An additional peak, of low intensity, can be observed at  $43.5^\circ$  (gray square), corresponding to metallic Cu (. JCPDS 003-1018). The formation of Cu impurities was also confirmed by EDX analysis, and it can be attributed to the reduction of  $\text{Cu}_2\text{O}$  during the synthesis in argon atmosphere, as also reported by Zhao et al. (Ref 47). Since the quantity of Cu is almost negligible, powders and

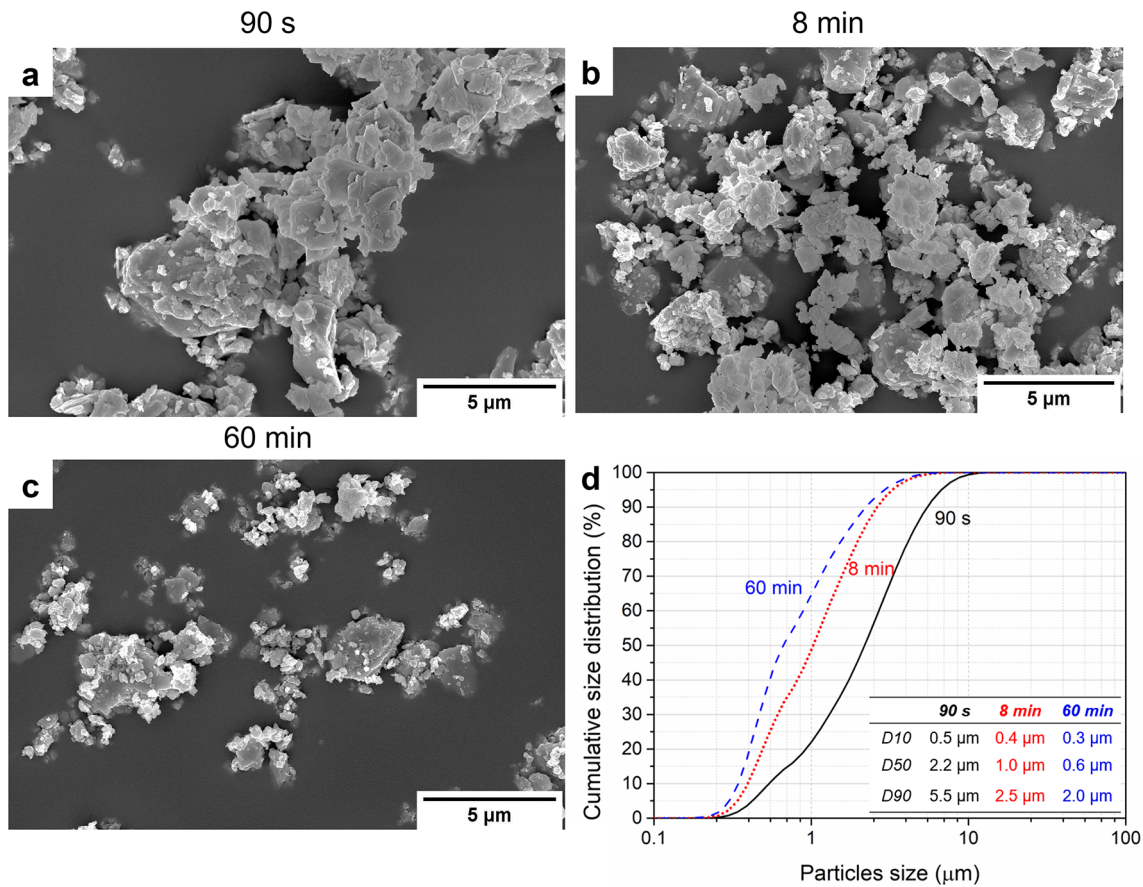


**Fig. 3** Morphologies of milled  $\text{CuFe}_2\text{O}_4$  powders, as given by SEM micrographs (SE mode, 10000 $\times$  magnification) after milling for (a) 90 s, (b) 8 min and (c) 60 min. The particle size distribution

curves and data of the powder batches are shown in (d). The black line corresponds to 90 s of milling, while the red dotted line refers to 8-min milling and the blue dashed line to the 60-min milled powders

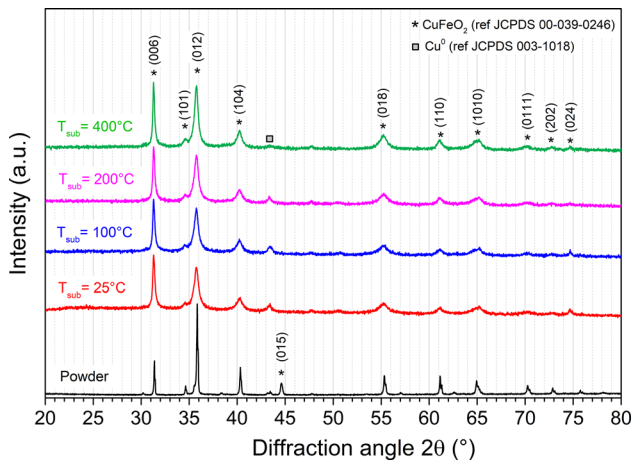


**Fig. 4** X-ray diffraction patterns of synthesized powder (black line) and coatings deposited with helium as process gas at  $2.9 \times 10^{-1}$  MPa at different substrate temperatures (25  $^{\circ}\text{C}$ , red line; 100  $^{\circ}\text{C}$ , blue line; 200  $^{\circ}\text{C}$ , pink lines; 40  $^{\circ}\text{C}$ , green lines). All coatings exhibit all the characteristic peaks of  $\text{CuFe}_2\text{O}_4$  with different relative intensities on the 006 and 012 planes. No trace of  $\text{CuFe}_2\text{O}_4$  is detected in the coatings

coatings were considered sufficiently pure for this work. Interestingly, the relative intensity of the two main peaks of  $\text{CuFe}_2\text{O}_4$  at 31.3 $^{\circ}$  and 35.7 $^{\circ}$ , corresponding to (006) and (012) crystallographic planes, respectively, notably differs between the powder and the substrate, indicating the presence of preferential orientation within the coatings or high lattice strain, as previously reported by Stocker et al. (Ref 46). Moreover, significant peaks broadening can be observed after the deposition for all substrate temperatures. Similar results have been obtained under different spraying conditions (gas pressure, gas type, powder), indicating substantial particle refinement during deposition. The entity of particle refinement and the coating texture were not quantitatively evaluated in the present work due to the complexity of the diffraction patterns, affected simultaneously by microstrains, preferential orientation and particle refinement. However, it will be further investigated in the future.

## Coatings Microstructures

### Nitrogen as Process Gas

The first sets of coatings were deposited on stainless steel substrates at room temperature. Figure 5 summarizes the SEM micrographs of  $\text{CuFeO}_2$  mono-layer coatings obtained by using nitrogen as process gas, at different gas flow/pressure settings (rows), and by using three powder batches with different median sizes—expressed as  $D_{50}$  (columns). For clarity of reading, black dotted lines highlight the interface between  $\text{CuFeO}_2$  and Pt layers deposited for SEM analysis.

The variation of spray parameter sets and powder sizes has significant influence on deposit microstructures. The comparison reveals that coating thickness increases with process gas pressure and decreasing powder sizes. Apart from that, an increased process gas pressure results also in slightly reduced porosity. Coarser particles ( $D_{50} = 2.2 \mu\text{m}$ ) tend to form irregular and discontinuous layers (Fig. 5a,d,g). In particular, low gas pressures ( $0.9 \times 10^{-1}$

MPa and  $1.6 \times 10^{-1}$  MPa) lead to low surface coverage with locally varying thickness (Fig. 5a,d), while increasing the gas pressure to  $2.9 \times 10^{-1}$  MPa improves the coating homogeneity (Fig. 5g). Finer feedstock powders ( $D_{50} = 1 \mu\text{m}$  and  $D_{50} = 0.6 \mu\text{m}$ ) result in complete surface coverage for all gas pressures (Fig. 5b,e,h and c,f,i). Generally, both sets of coatings exhibit high porosity (7–9%) for all gas pressures. In this case, increasing the gas pressure from  $0.9 \times 10^{-1}$  MPa to  $1.6 \times 10^{-1}$  MPa does not result in coating densification. On the contrary, coating porosity slightly decreases by increasing the gas pressure to  $2.9 \times 10^{-1}$  MPa. This effect is more pronounced for the thicker layers obtained by using the  $D_{50} = 0.6 \mu\text{m}$  feedstock powder, with porosity values varying from 8.5% (at  $0.9 \times 10^{-1}$  MPa pressure) to 7% (at  $2.9 \times 10^{-1}$  MPa pressure), and a microstructure consisting of few dense and compact areas, surrounded by more loosely bonded particles and large pores (Fig. 5c,f,i). Cu impurities are only rarely observed, in one of the coatings (Fig. 5g) such an impurity is highlighted by a red arrow. The different trends on layer build-up are compared in Fig. 6, showing the

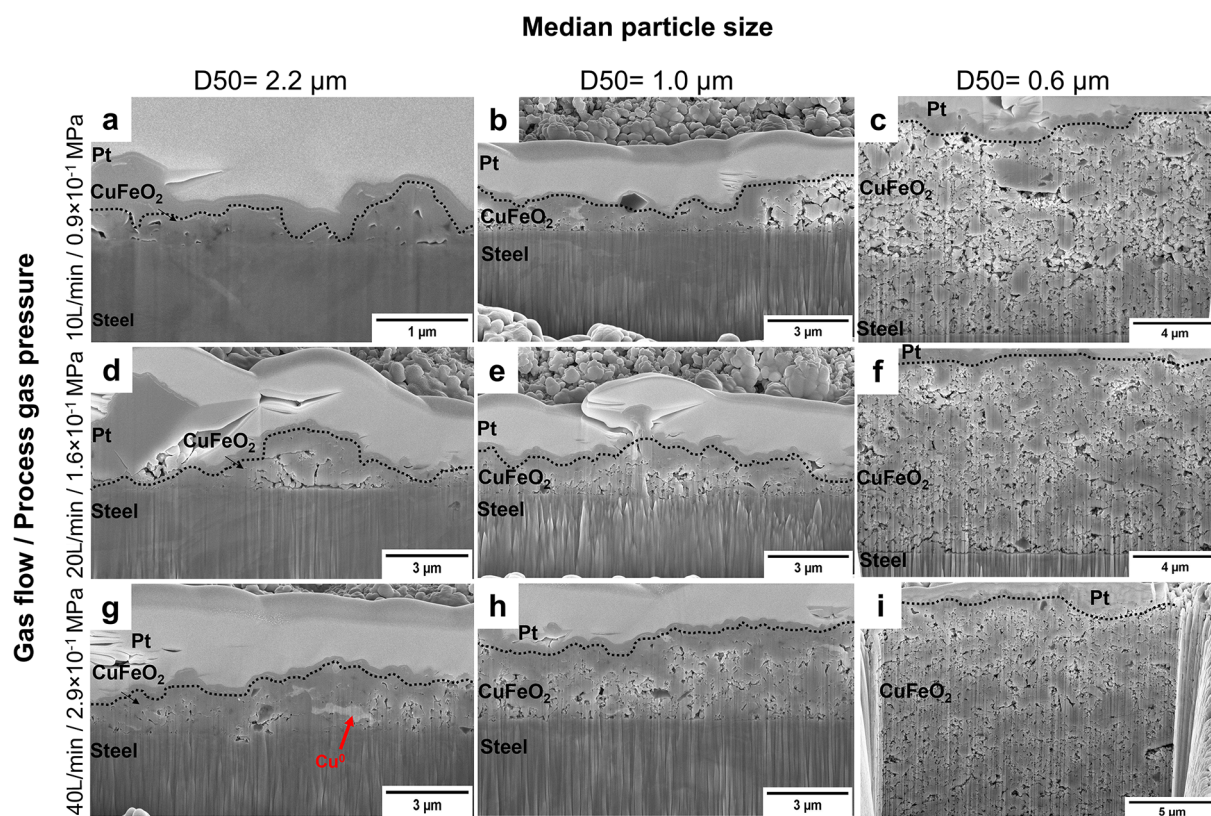


**Fig. 5** Coating microstructures as obtained under parameter variation. The monolayer coating cross sections for SEM micrographs (SE mode) were prepared by focused ion beam (FIB). The microstructures of  $\text{CuFeO}_2$  coatings sprayed with different gas flow/gas pressure (rows) and by using different powder batches (columns) are shown at different magnifications ( $12000 \times$ ,  $15000 \times$  or  $50000 \times$ ). Panels

(a,b,c) correspond to 10 L/min/ $0.9 \times 10^{-1}$  MPa, (d,e,f) refer to 20 L/min/ $1.6 \times 10^{-1}$  MPa, and (g,h,i) refer to 40 L/min/ $2.9 \times 10^{-1}$  MPa of gas flow/pressure. The black dotted lines highlight the interface between the coating and the Pt layers, while the red arrow indicates  $\text{Cu}^0$  impurities

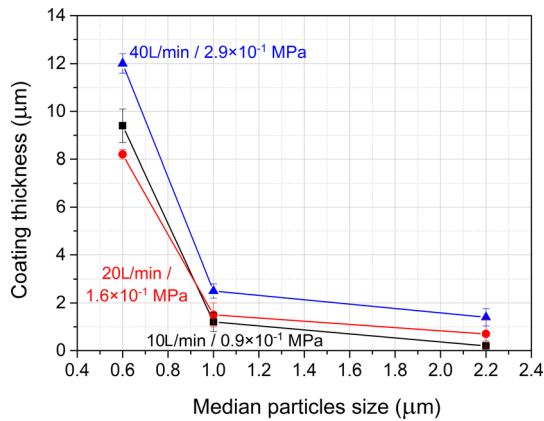


**Fig. 6** Coating thickness over median particle size ( $D_{50}$  values) for three different gas flow/pressure: 10 L/min/ $0.9 \times 10^{-1}$  MPa (black line and squares), 20 L/min/ $1.6 \times 10^{-1}$  MPa (red line and circles), 40 L/min/ $2.9 \times 10^{-1}$  MPa (blue lines and triangles)

coating thickness over the median particle sizes for different gas flows/pressures, clearly revealing the enhanced coating thickness by using smaller particles. In particular, by decreasing the median particle size from 2.2  $\mu\text{m}$  to 0.6  $\mu\text{m}$ , the coating thickness increases by a factor of  $\approx 6$ –8, depending on the gas flow/pressure. Generally, higher gas pressures result in thicker coatings, but the influence of gas pressure on layer build-up is more prominent for the coarser powders ( $D_{50} = 1.0, 2.2 \mu\text{m}$ ), more difficult to deposit. Increasing the gas pressure from  $0.9 \times 10^{-1}$  MPa to  $2.9 \times 10^{-1}$  MPa results in enhanced coating thickness by a factor of 7 or 2 for the coarser powders ( $D_{50} = 2.2 \mu\text{m}$  and  $D_{50} = 1 \mu\text{m}$ , respectively), instead of about 1.3 for the smallest one ( $D_{50} = 0.6 \mu\text{m}$ ).

Two- and four-layer coatings were deposited under the same spraying conditions of single layers. The comparison, here shown for one batch of powders ( $D_{50} = 1 \mu\text{m}$ ), indicates that the deposition of multi-layers and the increase in gas pressure do not reduce coating porosity. On the other hand, coating thickness increases with the number of layers, more prominently for higher gas pressure. The cross sections of multi-layer coatings sprayed with the  $D_{50} = 1 \mu\text{m}$  powder at different gas flow/pressure settings are shown in Fig. 7. Overall, the impact of two (Fig. 7a,c,e) or four (Fig. 7b,d,f) consecutive layers does not result in coating densification, with porosity ranging from 6 to 10% despite number of layers or gas pressure. Locally, larger dense areas are observed within the coating, but still surrounded by pores. This suggests that the impact of multiple layers may influence the densification by hammering effects to certain extent, but under here attained spraying conditions, this effect is not sufficient to properly consolidate the coating. As a consequence, the overall porosity is not significantly reduced compared to single layers. In addition, it can be noted that the four-layer coating sprayed

at  $2.9 \times 10^{-1}$  MPa (Fig. 7f) exhibits a highly defective microstructure, characterized by significantly large porosities (indicated by the blue arrows) and horizontal cracks (red arrows), further confirming that coating quality is not improved when multi-layers are deposited, not promoting particle consolidation and, at the same time, inducing stresses. Figure 8 shows the coating thickness over the number of layers for different gas flow/pressure settings. Given trends indicate a roughly linear increase of coating thickness with the number of layers. Extrapolating the data as linear correlation to the intersection with the abscissa (coating thickness = 0  $\mu\text{m}$ ) indicates that the deposition starts with an offset of 0.5 layers. This suggests that a certain surface activation is needed before coating building up and is in agreement with the formation of an anchoring layer before film consolidation and growth, as reported in the literature (Ref 38, 41). Trends in Fig. 8 also indicate that the increase in thickness is more pronounced for higher gas pressures. By spraying at  $0.9 \times 10^{-1}$  MPa, the coating thickness increases by a factor of 3 and 5.5 for two and four layers, respectively. Higher gas pressures ( $1.6 \times 10^{-1}$  and  $2.9 \times 10^{-1}$  MPa) further enhance the coating thickness: They form two-layer coatings which are  $\approx 3.7$  times thicker than single layers, while four-layer coatings have a mean thickness about 9 or 12 times higher than a monolayer sprayed at  $1.6 \times 10^{-1}$  and  $2.9 \times 10^{-1}$  MPa, respectively. Under the present spraying conditions, the  $\text{CuFeO}_2$  particles do not sufficiently deform and consolidate during deposition, resulting in porous and inhomogeneous coatings.

#### Helium as Process Gas

The same set of parameters was employed to deposit four-layer coatings by using helium as process gas onto stainless-steel substrates. This set of experiments served to evaluate within which ranges the coating quality could be improved by reaching significantly higher particle velocities. Figure 9 shows the cross sections of multi-layer coatings sprayed at different gas flow/pressure settings (rows) starting from different feedstock powders (columns). Using helium as process gas results in continuous and homogeneous coatings. The substrate/coating interfaces, when visible, are highly uniform. One exception is the coating obtained by spraying the coarser powder ( $D_{50} = 2.2 \mu\text{m}$ ) at the highest gas pressure ( $2.9 \times 10^{-1}$  MPa), where an interface crack is observed on the left part of the image (Fig. 9d), which here is probably triggered by Cu impurities. The red dashed line in Fig. 9(d) indicates the presence of interface and internal cracks, which propagate along the highly deformed Cu impurity, confirming that fracture can occur nearby the Cu/steel and Cu/ $\text{CuFeO}_2$  interfaces. In general, apart from higher thickness, the use

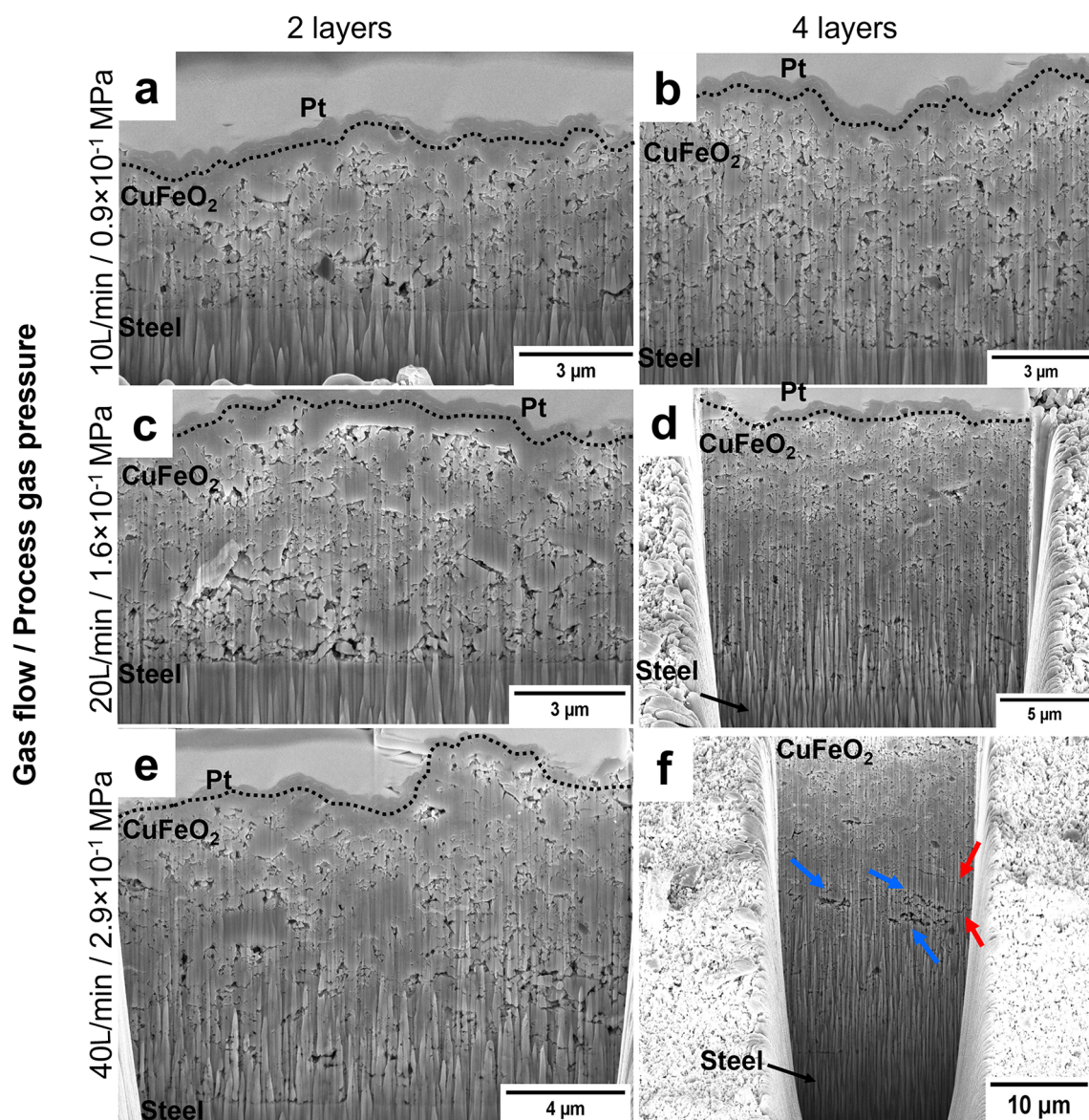


**Fig. 7** SEM micrographs (SE mode) of two- (a,c,e) and four- (b,d,f) layer coatings deposited by using the  $D_{50} = 1 \mu\text{m}$  powder batch. The cross sections were obtained by FIB. The microstructure of  $\text{CuFeO}_2$  coatings sprayed with different gas flow/pressure are shown at different magnifications ( $3500\times$ ,  $8000\times$ ,  $12000\times$  or  $15000\times$ ). Panels (a,b) correspond to  $10 \text{ L/min}/0.9 \times 10^{-1} \text{ MPa}$ , (c,d) refer to

$20 \text{ L/min}/1.6 \times 10^{-1} \text{ MPa}$  and (e,f) refer to  $40 \text{ L/min}/2.9 \times 10^{-1} \text{ MPa}$  of gas flow/pressure. The black dotted lines highlight the interface between the coating and the Pt layers, while the red arrows indicate the internal cracks and blue arrows indicate large porous areas

of helium also improves internal coating quality as compared to the samples sprayed with nitrogen as process gas. For all spraying conditions and powder sizes, the coatings show less porosity (compare Fig. 5 and 7). By using helium as process, the amounts of micron-sized pores sum up to about 3% or 2% for gas pressures of  $0.9 \times 10^{-1} \text{ MPa}$  and  $2.9 \times 10^{-1} \text{ MPa}$ , respectively. The associated better deformation for closing porosity can be attributed to the higher particle velocity when helium and higher gas pressures are used for deposition (Ref 40, 48). The attainable thickness of multi-layer coatings mainly depends on the

particle size: it increases from  $7 \mu\text{m}$  for coarser particles ( $D_{50} = 2.2 \mu\text{m}$ ) to  $27 \mu\text{m}$  for the finest ones ( $D_{50} = 0.6 \mu\text{m}$ ). No influence of gas pressure on coating thickness was observed.

#### Heated Substrates

One set of powder ( $D_{50} = 1 \mu\text{m}$ ) was selected to study the effect of substrate temperature during aerosol deposition. Thus, mono-layer coatings were deposited on stainless steel substrates heated to  $100^\circ\text{C}$ ,  $200^\circ\text{C}$  and  $400^\circ\text{C}$ . Due

to the high coating thickness, not allowing for suitable FIB preparation, cross sections were obtained by means of metallographic procedures (section “Analyses of phase composition and characterization of coating microstructures”). Figure 10 displays coating microstructures for different process gases and gas flows/pressures (rows) and increased substrate temperature (columns). At substrates temperatures of 100 and 200 °C using nitrogen as process

gas at  $0.9 \times 10^{-1}$  and  $2.9 \times 10^{-1}$  MPa results in highly inhomogeneous coatings in terms of thickness and microstructure. The coating thickness varies from 1-2  $\mu\text{m}$  to 12-18  $\mu\text{m}$  within the same layer, regardless of other spraying conditions. Increasing the substrate temperature to 400 °C at low gas pressure results in lower coating thickness ( $< 10 \mu\text{m}$ , Fig. 10c). Thus, no clear trend for coating thickness can be determined. The microstructural inhomogeneity refers to a range from highly porous to rather dense areas. Within the porous areas, undeformed particles can be observed, as highlighted by the red dashed lines in Fig. 10(a,b,d,f). In these areas, particle dimensions—ranging from 0.3  $\mu\text{m}$  to 2  $\mu\text{m}$ —are roughly comparable to the size distribution of the starting feedstock powder (see Fig. 3d, 8 min-milling powder), indicating negligible particle fragmentation upon impact. These features are more pronounced for low gas pressure ( $0.9 \times 10^{-1}$  MPa, Fig. 10(a,b)). For the deposition at substrate temperatures of 100 °C and 200 °C, increasing the pressure to  $2.9 \times 10^{-1}$  MPa slightly improved the degree of particle deformation, leading to the formation of locally denser areas (indicated by the red arrows), but the conditions are not sufficient to form coatings with uniformly low porosity (Fig. 10d,e). By using nitrogen as process gas, increasing the substrate temperature to 400 °C (Fig. 10f) does not have beneficial effects for coating formation. The lower particle fragmentation and deformation degree compared to the experiments with non-heated substrates (compare Fig. 5

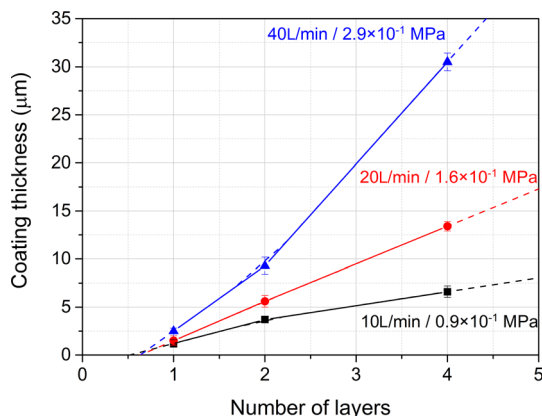


**Fig. 8** Coating thickness over the number of layers for the  $D_{50} = 1 \mu\text{m}$  powder batch, sprayed with different gas flow/pressure settings: 10 L/min/ $0.9 \times 10^{-1}$  MPa (black line and squares), 20 L/min/ $1.6 \times 10^{-1}$  MPa (red line and circles) and 40 L/min/ $2.9 \times 10^{-1}$  MPa (blue line and triangles). Dashed lines represent approximated linear fits and the extrapolation to the intersection with the abscissa for coating thickness = 0  $\mu\text{m}$

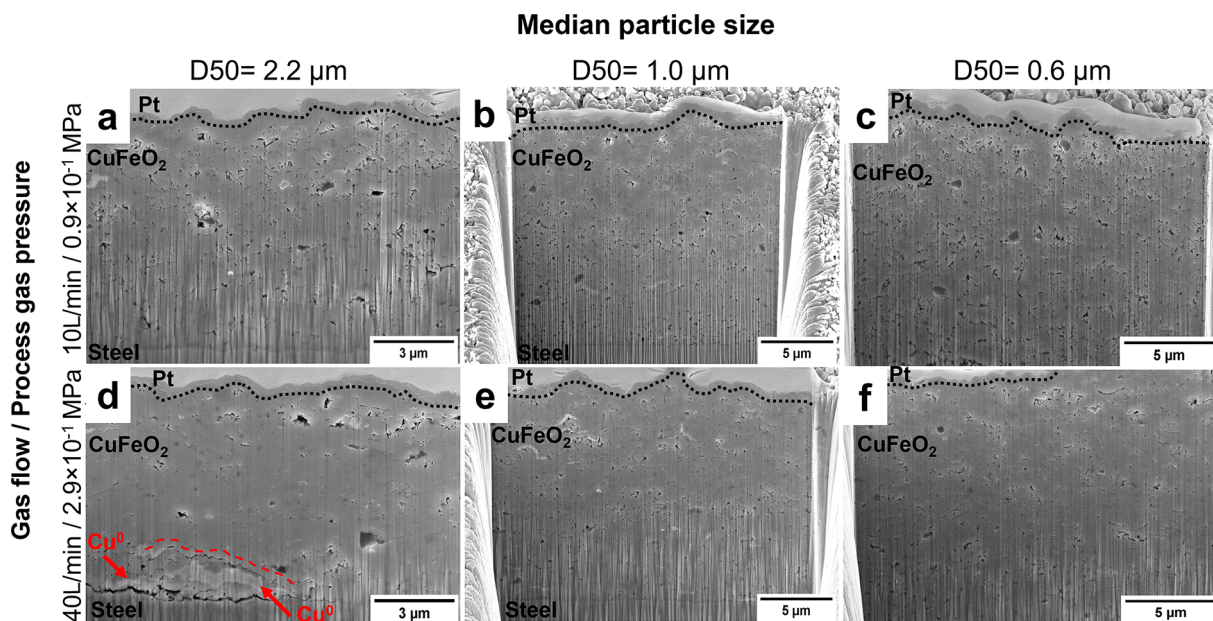


**Fig. 9** Microstructures of multi-layer  $\text{CuFeO}_2$  coatings sprayed by using helium as process gas. The cross sections were obtained by FIB. The SEM micrographs (SE mode) at 10000 $\times$  or 15000 $\times$  magnification of the four-layer coatings are arranged according to different gas flow/pressure settings (rows) and feedstock powders (columns).

Panels (a,b,c) correspond to the lowest gas flow/pressure, i.e., 10 L/min/ $0.9 \times 10^{-1}$  MPa, and (d,e,f) to the highest gas flow/pressure, i.e., 40 L/min/ $2.9 \times 10^{-1}$  MPa. The black dotted lines highlight the interface between the coating and the Pt layers, while the red dotted lines indicate the internal cracks along a  $\text{Cu}^0$  impurity (red arrows)

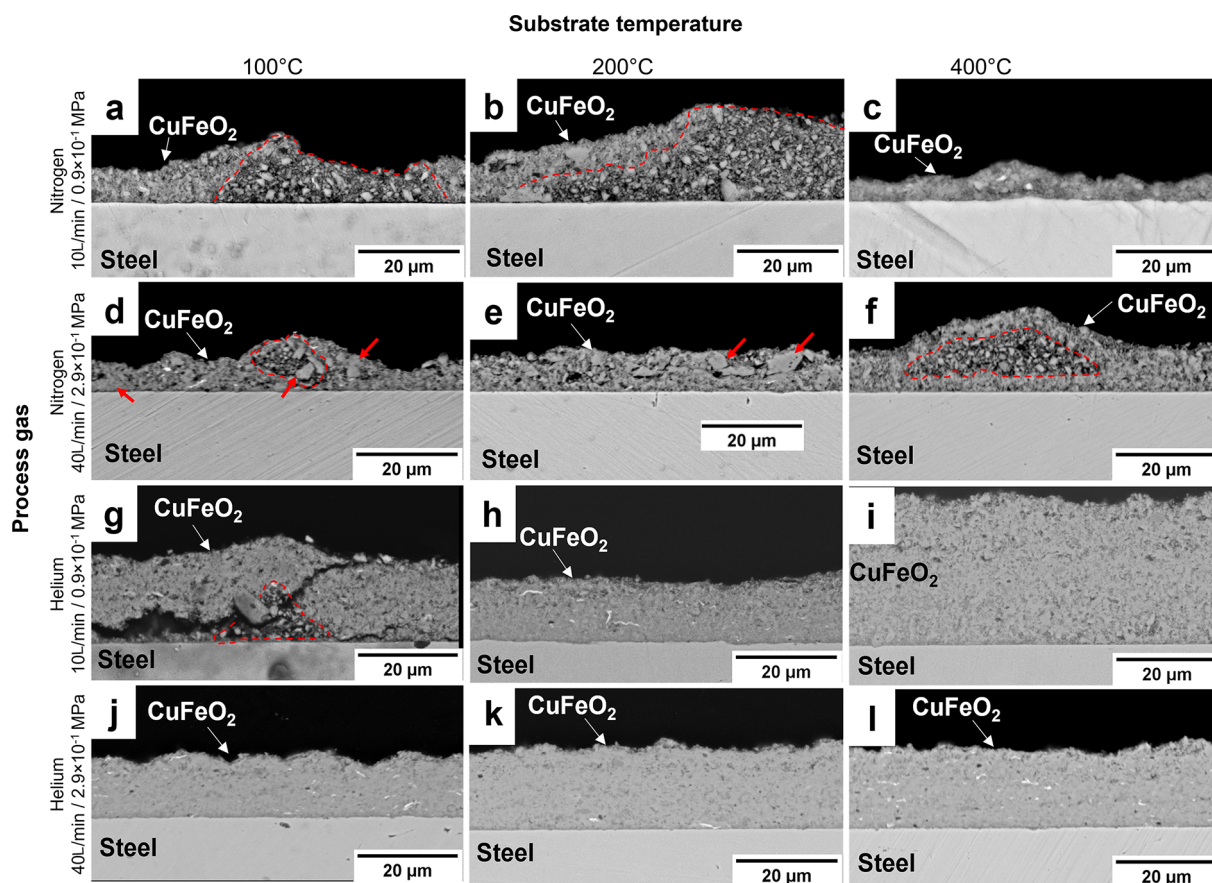


**Fig. 10** Microstructures of mono-layer coatings sprayed onto heated stainless steel substrates. The cross sections were obtained by means of metallographic preparation. The SEM micrographs (SE mode) at 4000 $\times$  magnification are arranged according to different substrate temperatures (columns) and different process gas and gas flow/pressure settings (rows). Panels (a,b,c) correspond to spraying with

nitrogen at 10 L/min/ $0.9 \times 10^{-1}$  MPa, (d,e,f) to nitrogen at 40 L/min/ $2.9 \times 10^{-1}$  MPa, (g,h,i) refer to spraying with helium at 10 L/min/ $0.9 \times 10^{-1}$  MPa, and (j,k,l) to helium at 40 L/min/ $2.9 \times 10^{-1}$  MPa. The red dashed lines indicate clusters of undeformed particles, while the red arrows point to the denser areas

and 10), may be attributed to particles impacting on softer surfaces due to heating. While lower particle/substrate hardness ratio can improve the film anchoring (Ref 49), lower deceleration by hitting a softer surface may prevent efficient particle deformation and fracturing. Enhancing the particle velocity by changing the gas pressure is not sufficient to attain good coating quality.

On the other hand, when helium is used as process gas, poorly deformed particles can only be observed for the coating sprayed at 100  $^{\circ}\text{C}$  and  $0.9 \times 10^{-1}$  MPa (Fig. 10g). In this case, all the undeformed particles are smaller than 1  $\mu\text{m}$ , indicating a partial fragmentation. It can be reasonably supposed that the crack formation at the coating/substrate interface and within the coating is caused by such loosely bonded particles. In contrast, all other spraying conditions lead to continuous and homogeneous coatings with low porosity. Porosity is reduced from 5 to 3% by increasing the gas pressure from  $0.9 \times 10^{-1}$  to  $2.9 \times 10^{-1}$  MPa, while substrate temperature has no discernible effect on coating porosity and thickness. The remarkably high

thickness ( $\approx 27 \mu\text{m}$ ) of the  $\text{CuFeO}_2$  coating deposited with helium as process gas at 40 L/min at 400  $^{\circ}\text{C}$  (Fig. 10i) probably is the result of non-steady powder flow during spraying.

In general, for both carrier gas types, the coating build-up onto heated substrates does not follow a specific trend. To some instance, this may be attributed to poorly adhering particles, which are more prone to erosion.

### Impact Morphology and Adhesion of Single Particles

Investigating the main features of individual particle impact morphologies can provide valuable information on deformation and bonding under varying impacting conditions. Figure 11 summarizes typical features of single-impact particles obtained under perspective view of the SEM (tilt angle of 52 $^{\circ}$ ) obtained by spraying different feedstock powders (columns) with nitrogen or helium as process gas at different gas flow/pressure settings (rows). General

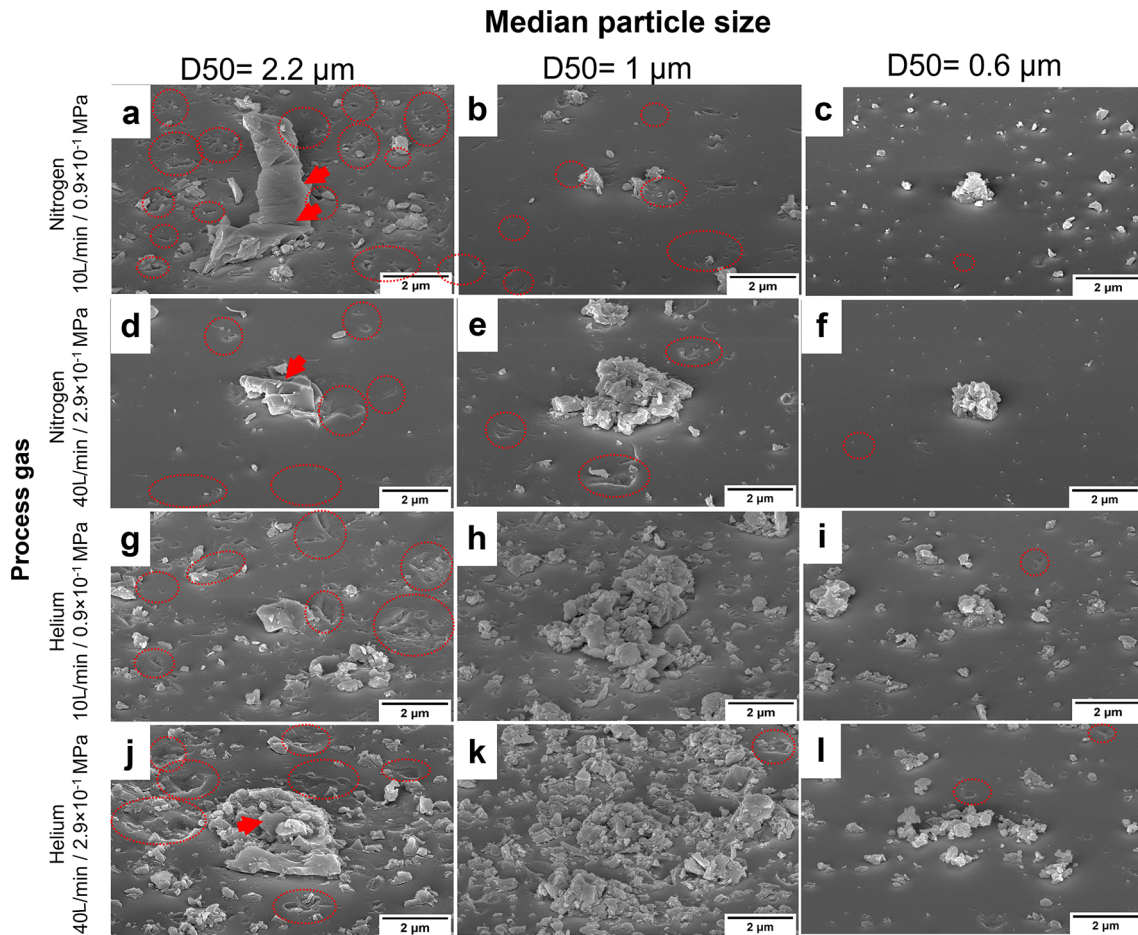


**Fig. 11** Single-particle impact morphologies under tilted view ( $52^\circ$ ) of SEM images (SE mode) at  $20000\times$  magnification as obtained by spraying on stainless steel substrates with different process gases and gas flow/pressure settings (rows) and by using different powder batches (columns). Panels (a,b,c) correspond to spraying with nitrogen at  $10\text{ L/min}/0.9 \times 10^{-1}\text{ MPa}$ , (d,e,f) refer to spraying with

nitrogen at  $40\text{ L/min}/2.9 \times 10^{-1}\text{ MPa}$ , (g,h,i) correspond to spraying with helium as process gas at  $10\text{ L/min}/0.9 \times 10^{-1}\text{ MPa}$ , and (j,k,l) refer to spraying with helium at  $40\text{ L/min}/2.9 \times 10^{-1}\text{ MPa}$ . The red arrows indicate particles with internal deformation, while red dotted lines underline the craters formed on the substrate surface

differences concern the amounts of bonded particles and empty craters, possible fragment sizes and types of failure. In brief comparison, the number of bonded particles or fragments increases with decreasing powder sizes and switching from nitrogen to helium as process gas. For better illustration, the red dotted circles in Fig. 11 indicate the presence of craters in the substrate surface caused by non-successful impacts. The number of empty craters increases when coarser particles ( $D_{50} = 2.2\ \mu\text{m}$ ) are deposited (Fig. 11a,d,g,j). When helium is used as process gas, the number of craters is lower, but, if present, their sizes are bigger than by using nitrogen as process gas. Crater dimensions nearly approach the original powder sizes ( $D_{50} = 2.2\ \mu\text{m}$ ) when such coarse particles are sprayed with helium at  $2.9 \times 10^{-1}\text{ MPa}$ , reaching a maximum lateral size of  $1.5\ \mu\text{m}$  (Fig. 11j). On the contrary, only few and small indents can be observed on the substrate surface when the  $D_{50} = 1\ \mu\text{m}$  powder is deposited with

nitrogen (Fig. 11b,e). Higher rates of successful impacts are obtained by (i) using helium as process gas (Fig. 11h,k) or by (ii) spraying the finer powder ( $D_{50} = 0.6\ \mu\text{m}$ , Fig. 11c,f,i,l), as the number of bonded particles remarkably increases and almost no sign of rebounding is observed for these samples. However, for all spraying conditions, most of the adhering particles exhibit a fractured angular morphology and dimensions that are smaller than the feedstock sizes. The number of fragments decreases with particle sizes. Table 3 summarizes respective data as minimum and maximum values. This indicates that particles can successfully fracture upon impact, forming nano-sized fragments. Only few coarse particles are retained after impact (Fig. 11a,g,j). As highlighted by the red arrows, these particles show signs of internal deformation, suggesting that they can deform to a certain extent, without flattening or fracturing. However, the number of particles that show sorts of internal deformation

is rather low. Most prominently, bonding is either associated with adhesion of small particles or fragments.

The effect of substrate temperature was investigated for one batch of powders ( $D_{50} = 1 \mu\text{m}$ ). Figure 12 shows SEM images in perspective views (tilt angle of  $52^\circ$ ) of particles

sprayed on heated substrates (columns) by using different process gases and gas flow/pressure settings (rows). As compared to the situation for non-heated substrates, the major difference concerns the overall less prominent occurrence of empty craters and lower particle deformation

**Table 3** Size ranges (minimum–maximum values) of  $\text{CuFeO}_2$  fragments formed during single-particle impacts of  $D_{50} = 2.2 \mu\text{m}$ ,  $D_{50} = 1 \mu\text{m}$  and  $D_{50} = 0.6 \mu\text{m}$  powders on stainless steel substrates

	$D_{50} = 2.2 \mu\text{m}$ , (nm)	$D_{50} = 1 \mu\text{m}$ , (nm)	$D_{50} = 0.6 \mu\text{m}$ , (nm)
Nitrogen 10 L/min, $0.9 \times 10^{-1}$ MPa	150-1000	60-800	20-600
Nitrogen 40 L/min, $2.9 \times 10^{-1}$ MPa	140-900	80-900	20-600
Helium 10 L/min, $0.9 \times 10^{-1}$ MPa	150-1000	40-800	20-800
Helium 40 L/min, $2.9 \times 10^{-1}$ MPa	60-1000	40-1000	20-600

The data were determined for varied spraying conditions by using nitrogen or helium as process gas at different gas pressures. Possible agglomerates were excluded from the dimensional ranges

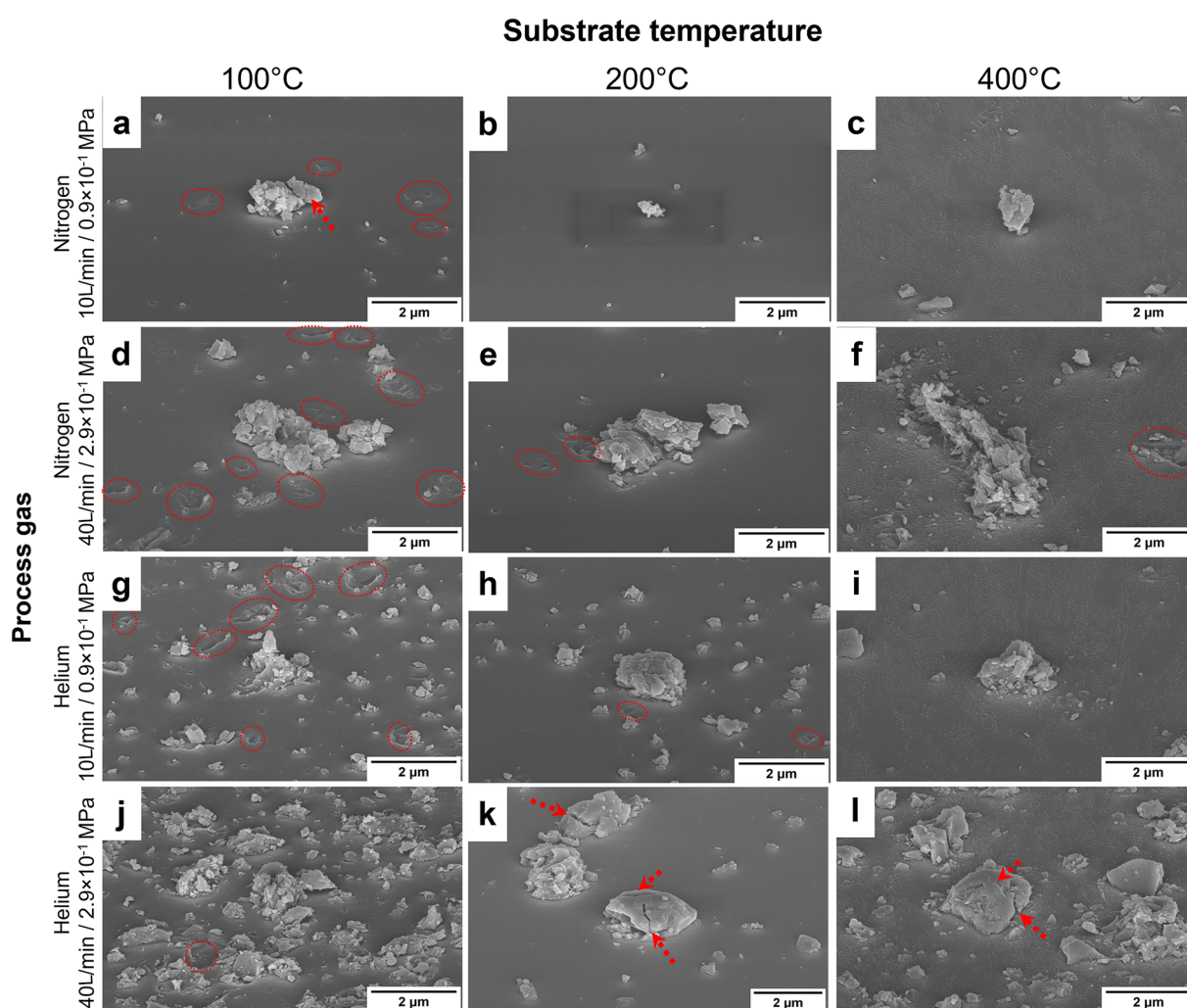


**Fig. 12** Single-particle impact morphologies under tilted view ( $52^\circ$ ) of SEM images (SE mode) at  $20000 \times$  magnification as obtained by spraying on stainless steel substrates with different process gases and gas flow/pressure settings (rows) at different substrate temperatures (columns). Panels (a,b,c) correspond to spraying with nitrogen at 10 L/min/ $0.9 \times 10^{-1}$  MPa, (d,e,f) refer to spraying with nitrogen at

40 L/min/ $2.9 \times 10^{-1}$  MPa, (g,h,i) correspond to spraying with helium at 10 L/min/ $0.9 \times 10^{-1}$  MPa, (j,k,l) refer to spraying with helium at 40 L/min/ $2.9 \times 10^{-1}$  MPa. The red dotted arrows highlight cracks within the particles, while red dotted lines underline the craters formed on the substrate surface

and fragmentation. Nevertheless, small craters can be observed for several types of samples, as highlighted by red dotted circles (Fig. 12a,d,e,f,g,h,j). For all spraying conditions, the number of craters decreases with the substrate temperature, suggesting that substrate heating may have a beneficial effect on particle adhesion. When the substrate is heated to 200 and 400 °C, retained coarse particles in original size can be observed (Fig. 12e,f,h,i,k,l). Particles sprayed with nitrogen or low gas pressure ( $0.9 \times 10^{-1}$  MPa) do not show significant signs of fracture or deformation (Fig. 12e,f,h,i). On the other hand, when helium is employed as process gas at high pressure ( $2.9 \times 10^{-1}$  MPa), cracks can be observed within the coarse particles (red dotted arrows in Fig. 12(k,l)). This may be attributed to the higher particle velocities, and regimes of stress concentration under deceleration, that on softened surfaces cause crack formation, but are still insufficient to ensure particle crushing. In summary, substrate heating appears to support adhesion, but avoids particle fragmentation and deformation upon impact. This is also confirmed by the dimensional ranges of particles shown in Table 4. Bonded particles are of the same size range as the starting feedstock powder and, even when fragments are formed, they are always larger than 100 nm, while depositing the same powder batch—under equal spraying conditions—on room-temperature substrates promoted the formation of smaller fragments < 100 nm (compare Tables 3 and 4).

**Thin Films Microstructure**

For the final application, thin, dense and well-bonded coatings are required. On the one hand, the layer thickness should exceed the minimum value required to absorb the incident light, usually on the order of the optical penetration depth ( $\alpha^{-1}$ ). On the other hand, excessive thickness may enhance losses by charge carrier recombination (Ref 15). Therefore, coating thickness should be finely tuned for a given photoelectrode material, generally < 1 µm. In addition, high porosity and interface defects can cause ohmic losses, resulting in poor efficiency. To fulfil the requirements for suitable photocathode thin films, parameters for aerosol deposition were tuned according to the previous results (see section “Coatings microstructures”

and section “Impact morphology and adhesion of single particles”) and are summarized in Table 2. The two finer powder batches ( $D_{50} = 1 \mu\text{m}$  and  $D_{50} = 0.6 \mu\text{m}$ ) were sprayed on FTO-glass substrates at room temperature. Both nitrogen and helium were used as process gas at high pressure ( $2.9 \times 10^{-1}$  MPa). In order to reduce the coating thickness, a systematic variation of the feeding rate, line distance, traverse speed and the application of cyclones was carried out. The combination of varying the feeding rate and the line distance (i) and the application of cyclones while changing the traverse speed (ii) were selected to be discussed in detail.

*Varying the Feeding Rate and Line Distance*

Figure 13 shows the microstructures of the thin films obtained by spraying  $D_{50} = 0.6 \mu\text{m}$  powders at different feeding rate (columns) and line distance (rows) by using nitrogen as process gas at a pressure of  $2.9 \times 10^{-1}$  MPa. Using low feeding rates results in rather discontinuous coatings for all conditions. The example of a feeding rate of  $1 \text{ cm}^3/\text{h}$  leads to incomplete layer formation (Fig. 13a,c). When a line distance of 1 mm is employed, only few bonded particles can be observed (Fig. 13a). Higher surface coverage can be reached by increasing the line distance to 2 mm. However, the layer thickness is extremely discontinuous, ranging from 0 to 730 nm (Fig. 13c). For a feeding rate of  $2 \text{ cm}^3/\text{h}$ , complete surface coverage is obtained for both line distance values (Fig. 12b,d). However, in the case of a line distance of 1 mm, the coating locally shows a crack at the interface the FTO-glass substrates. For both conditions, the layer thickness varies, here within ranges from 350 to 1400 nm for the 1 mm line distance (Fig. 13b) and from 120 to 800 nm for the 2 mm line distance (Fig. 13d).

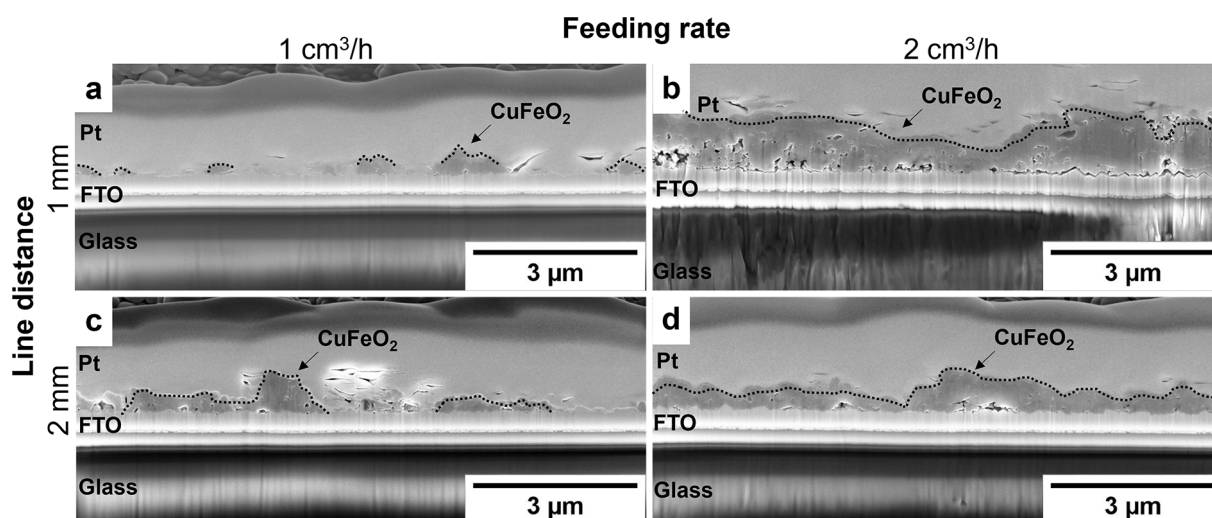
*Applying Cyclones as Particle Filter and Varying the Traverse Speed*

Figure 14 and 15 show the microstructure of thin films obtained by adding the Z1000 and Z500 cyclones placed in sequence within the process gas feed line and by changing the traverse speed. Figure 14 refers to thin films obtained

**Table 4** Size ranges (minimum–maximum values) of CuFeO<sub>2</sub> fragments formed during single-particle impacts of  $D_{50} = 1 \mu\text{m}$  powder on stainless steel substrates heated to 100, 200 and 400 °C

	Substrate temperature		
	100 °C, (nm)	200 °C, (nm)	400 °C, (nm)
Nitrogen 10 L/min, $0.9 \times 10^{-1}$ , MPa	100-1000	100-600	300-1000
Nitrogen 40 L/min, $2.9 \times 10^{-1}$ , MPa	400-1000	300-1300	100-1000
Helium 10 L/min, $0.9 \times 10^{-1}$ , MPa	150-1000	200-1200	200-1200
Helium 40 L/min, $2.9 \times 10^{-1}$ , MPa	120-1000	200-1400	100-1400

Possible agglomerates were excluded from the dimensional ranges.



**Fig. 13** FIB-SEM micrographs (SE mode) at  $15000\times$  magnification of thin films sprayed onto FTO-glass substrates with different feeding rate (columns) and at different line distance (rows). Feeding rates and line distances of (a)  $1\text{ cm}^3/\text{h}$  and  $1\text{ mm}$ , (b)  $2\text{ cm}^3/\text{h}$  and  $1\text{ mm}$ , (c)  $1$

$\text{cm}^3/\text{h}$  and  $2\text{ mm}$ , (d)  $2\text{ cm}^3/\text{h}$  and  $2\text{ mm}$  were employed, respectively. The coatings were sprayed by using nitrogen as process gas at a gas flow/pressure of  $40\text{ L}/\text{min}/2.9 \times 10^{-1}\text{ MPa}$

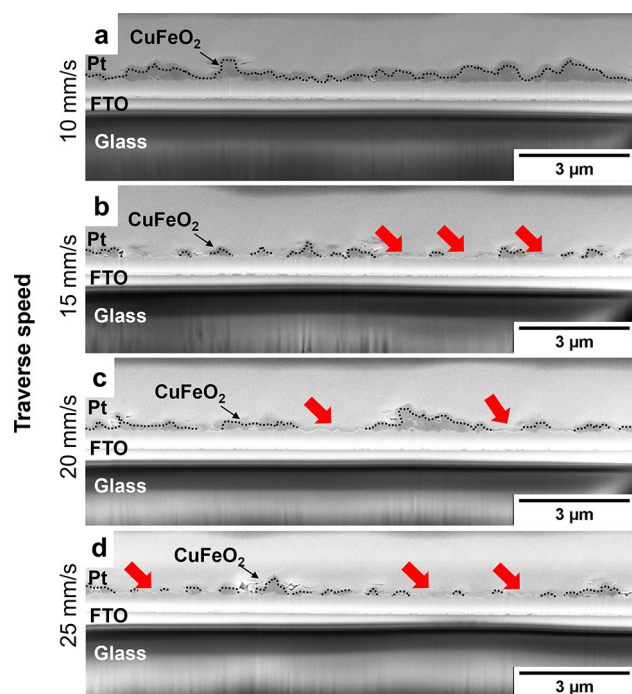


**Fig. 14** FIB-SEM micrographs (SE mode) at  $15000\times$  magnification of thin films sprayed on FTO-glass substrates using the  $D_{50} = 0.6\text{ }\mu\text{m}$  powder, filtered by two cyclones in the process gas feeding line and by varying the traverse speed. Traverse speeds of (a)  $10\text{ mm}/\text{s}$ , (b)  $15\text{ mm}/\text{s}$ , (c)  $20\text{ mm}/\text{s}$  and (d)  $25\text{ mm}/\text{s}$  were used for spraying with nitrogen as process gas at a gas flow/pressure of  $40\text{ L}/\text{min}/2.9 \times 10^{-1}\text{ MPa}$

by spraying the  $D_{50} = 0.6\text{ }\mu\text{m}$  powder with nitrogen as process gas at  $2.9 \times 10^{-1}\text{ MPa}$ , while Fig. 15 shows the microstructure of thin films obtained by spraying the  $D_{50} = 1\text{ }\mu\text{m}$  and  $D_{50} = 0.6\text{ }\mu\text{m}$  powders (columns) at

different traverse speeds (rows) using helium as process gas. When using nitrogen as process gas, a continuous and thin layer can only be obtained at traverse speed of  $10\text{ mm}/\text{s}$  (Fig. 14a). For higher speeds, uncomplete surface coverage is observed, as several uncoated areas can be observed on the FTO-glass substrates, as highlighted by the red arrows in Fig. 14(b,c,d). By contrast, complete surface coverage and continuous layers are obtained for all traverse speeds when helium is used as process gas (Fig. 15). Both powder batches ( $D_{50} = 1\text{ }\mu\text{m}$  and  $D_{50} = 0.6\text{ }\mu\text{m}$ ) form thin coatings with low porosity (Fig. 15). In this case, by reducing the number of particles that impact on a surface unit per unit time, higher traverse speeds result in lower coating thickness. Moreover, at same kinematic parameter sets, coatings based on the coarser powder have slightly lower thickness than the ones sprayed with the finer size distribution, in agreement to previous results (see section “Coatings microstructures”). SEM micrographs in Fig. 15(a,c,e,g) show that feeding rates of  $10$ ,  $15$ ,  $20$  and  $25\text{ mm}/\text{s}$  result in coating thickness values of  $610 \pm 120\text{ nm}$ ,  $500 \pm 150\text{ nm}$ ,  $320 \pm 70\text{ nm}$  and  $190 \pm 60\text{ nm}$ , respectively, when using the  $D_{50} = 1$  powder. Systematically higher thickness values, ranging from  $310 \pm 140\text{ nm}$  for  $25\text{ mm}/\text{s}$  to  $980\text{ nm} \pm 110\text{ nm}$  for  $10\text{ mm}/\text{s}$ , were instead obtained with the  $D_{50} = 0.6\text{ }\mu\text{m}$  powder (Fig. 15b,d,f,h). Due to the high standard deviation associated with the mean thickness values, no deeper considerations can be made. Apart from higher thickness, the coatings obtained using the  $D_{50} = 0.6\text{ }\mu\text{m}$  powder also show slightly higher porosity than the ones sprayed with the coarser batch. In the former case, coating porosity varies from  $2.3$  to  $4\%$  depending on the traverse speed. On

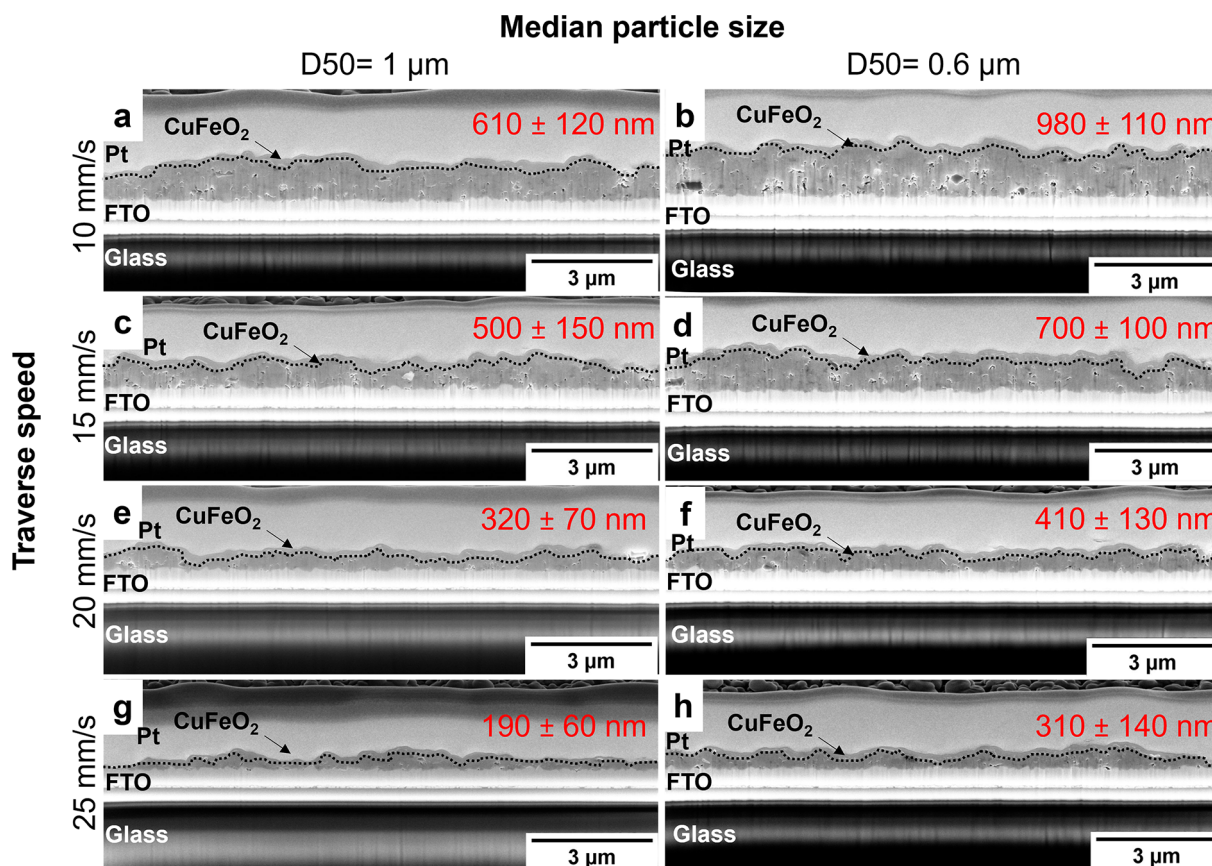


**Fig. 15** FIB-SEM micrographs (SE mode) at 15000 $\times$  magnification of thin films sprayed on FTO-glass substrates by using different feedstock powders (column), filtered by two cyclones in the process gas feeding line, and different traverse speeds (rows). Traverse speeds

of (a,b) 10 mm/s, (c,d) 15 mm/s, (e,f) 20 mm/s and (g,h) 25 mm/s were used for spraying the  $D_{50} = 1 \mu\text{m}$  (a,c,e,g) and  $D_{50} = 0.6 \mu\text{m}$  (b,d,f,h) powders. The coatings were sprayed by using helium as process gas and a gas flow/pressure of 40 L/min/ $2.9 \times 10^{-1}$  MPa

the other hand, coatings obtained by spraying the  $D_{50} = 1 \mu\text{m}$  powders exhibit porosity ranges between 1.6 and 3.7% and, as far as detectable, porosity does not vary with the traverse speeds.

### Optical Properties

By aspects of ensuring lower porosity, the thin films sprayed with  $D_{50} = 1 \mu\text{m}$  powder by using helium as process gas and a gas pressure of  $2.9 \times 10^{-1}$  MPa were selected for additional testing. In order to evaluate the influence of thickness on the functional coating properties, samples sprayed with three traverse speeds (10, 20 and 25 mm/s) were chosen. Reflectance (a,c) and transmittance (b,d) spectra of the selected thin films are shown in Fig. 16. The spectra are collected in the visible and near-infrared (NIR) regions for coatings in the “as-sprayed” state with thickness of  $190 \pm 60$  nm,  $320 \pm 70$  nm and  $610 \pm 120$  nm (Fig. 16a,b) and after annealing in air at  $550 \text{ }^\circ\text{C}$  (Fig. 16c,d). General coating appearance before and after annealing is shown in the small inserts in Fig. 16, containing macropictures of  $320 \pm 70$  nm coatings as an

example. The optical properties of as-sprayed  $\text{CuFeO}_2$  coatings slightly change with coating thickness. The percentage of reflected light is constant for all samples, ranging from 20% at  $\lambda_{1400\text{nm}}$  to 6% over the entire visible range ( $< \lambda_{700\text{nm}}$ ). In contrast, the amount of transmitted light is slightly lower for the thicker coatings. The light transmission of the thinnest coating ( $190 \pm 60$  nm) ranges from a maximum of 50% in the NIR range to 16-7.5% in the visible one ( $\lambda_{700\text{nm}}-\lambda_{400\text{nm}}$ ). For thicker coatings, the percentage of transmitted light is slower and decreases from a maximum of 42% in the NIR range to  $\leq 6\%$  below  $\lambda_{700\text{nm}}$ . However, all films can absorb high amounts of the visible light, roughly estimated with Eq.2 at two wavelengths ( $\lambda_1 = 400$  nm and  $\lambda_2 = 700$  nm):

$$A(\%)_{\lambda} = 100\% - R(\%)_{\lambda} - T(\%)_{\lambda}$$

and corresponding to 78-86, 91-93 and 86-88% for the  $190 \pm 60$ ,  $320 \pm 70$  and  $610 \pm 120$  nm samples, respectively.

By annealing in air,  $\text{CuFeO}_2$  coatings slightly change in color, indicating a change in the optical properties. This is confirmed by the variation in the percentage of reflected

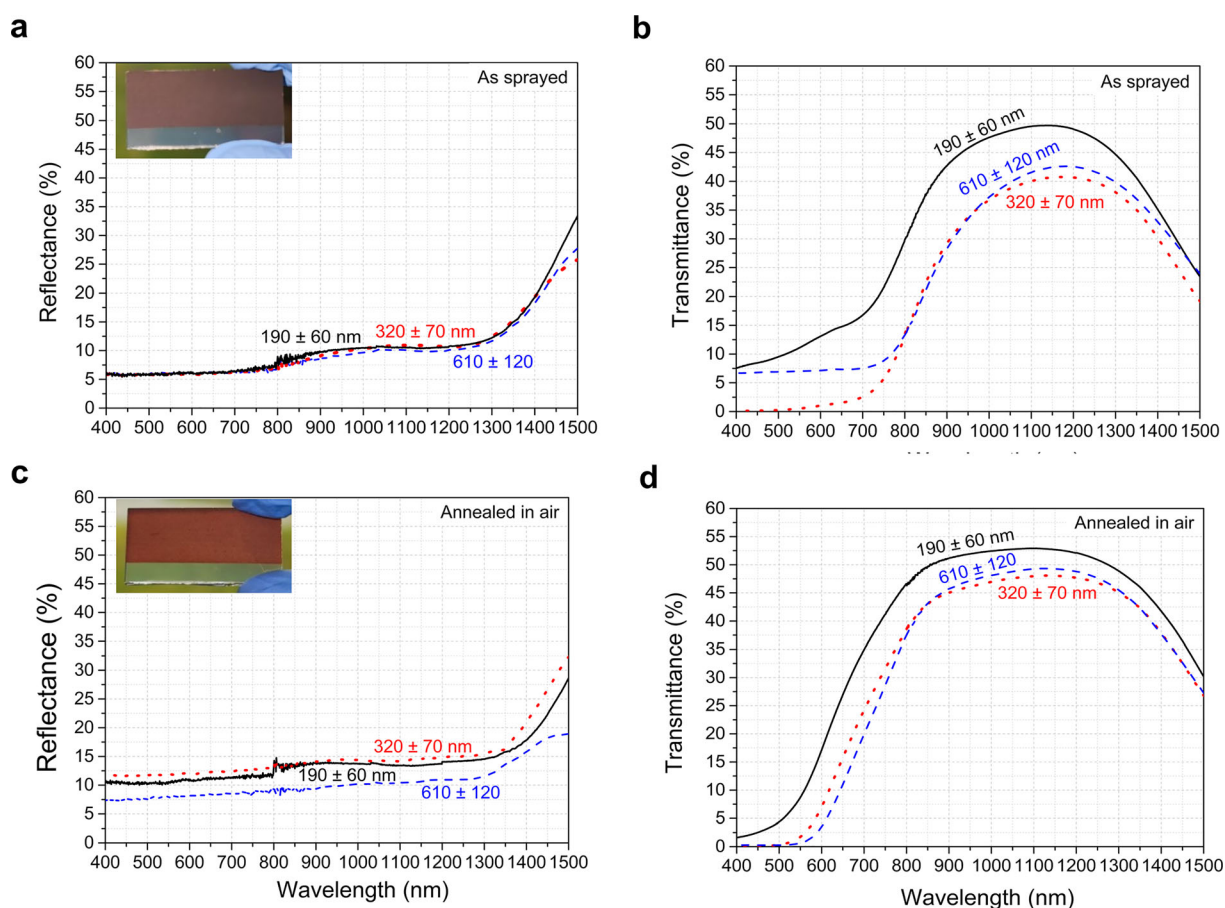


**Fig. 16** UV-Vis-NIR spectra of the total reflected (a,c) and transmitted (b,d) light by the  $\text{CuFeO}_2$  thin films in the (a,b) as-sprayed condition and (c,d) after annealing in air at  $550^\circ\text{C}$  for 1 h. Black lines correspond to samples with thickness of  $190 \pm 60$  nm (sprayed at  $25$  mm/s), red dotted lines to  $320 \pm 70$  nm thick samples (sprayed at  $20$  mm/s) and blue dashed lines to  $610 \pm 120$  nm thick

light, which increases for all coatings:  $R$  (%) ranges from  $\approx 7\%$  for the thickest coating ( $610 \pm 120$  nm) to 11–12% for the thinner ones at  $\lambda \leq 700$  nm. On the other hand, after the thermal treatment, the amount of transmitted light only increases for wavelengths above  $600$  nm. For  $\lambda \leq 550$  nm, lower quantities of the visible light are transmitted with  $T$  (%) varying from 1 to 2% for the  $610 \pm 120$  nm and  $320 \pm 70$  nm samples to 2–7% for the thinner one ( $190 \pm 60$  nm). The resulting ranges of absorbed visible light ( $A\%$ ) are therefore broader and shifted toward lower ranges: 54–87, 63–87 and 72–91% for the  $190 \pm 60$ ,  $320 \pm 70$  and  $610 \pm 120$  nm sample, respectively. As a rough estimation of  $A$  (%), these results mainly show that all coatings can absorb at least half of the total visible light. Moreover, the shape of reflectance and transmittance spectra shows that optical transitions occur within the coatings over the scanned range: Reflectance and transmittance spectra exhibit a gradual decrease in the visible range, probably corresponding to a substantial

increase in the absorbance. High absorption in the visible range has also been reported by other authors for  $\text{CuFeO}_2$  thin films obtained by reactive magnetron sputtering or sol-gel methods, although steeper or multiple absorption edges were sometimes observed in the 300–800 nm range (Ref 50–52).

### Photoelectrochemical Performance and Chemical Stability of the Coatings

The photoelectrochemical performance and chemical stability of the thin films were tested by means of chronoamperometry. During this test, a constant potential of  $+0.44$  V vs RHE was applied for 600 s under chopped illumination in 1 M NaOH, and the response of the  $\text{CuFeO}_2$  electrodes was measured in terms of photocurrent density ( $J_{\text{ph}}$ ). The  $J_{\text{ph}}$  corresponds to the rate of charge carrier generation for a specific active area, and it is proportional to the amount of generated  $\text{H}_2$ . The variation over

time of the photocurrent density can provide information on the chemical stability of the electrode.

Figure 17 shows the photocurrent density curves of the selected coatings in the as-sprayed (a) and air-annealed (b) conditions. Black, red and blue curves correspond to different coating thickness of  $190 \pm 60$ ,  $320 \pm 70$  and  $610 \pm 120$  nm, respectively. All as-sprayed samples generate low photocurrents, which slightly decrease over time (Fig. 17a). The photocurrent values are not proportional to the film thickness, in the first 60 s of testing here varying from  $10 \mu\text{A}/\text{cm}^2$  for the thinner coating ( $190 \pm 60$  nm) to 5.5 and  $7.5 \mu\text{A}/\text{cm}^2$  for the  $320 \pm 70$  nm and  $610 \pm 120$  nm ones, respectively. The  $J_{\text{ph}}$  values gradually vary until reaching minimum values of  $8.4 \mu\text{A}/\text{cm}^2$  ( $190 \pm 60$  nm),  $3.8 \mu\text{A}/\text{cm}^2$  ( $320 \pm 70$  nm) and  $6.8 \mu\text{A}/\text{cm}^2$  ( $610 \pm 120$  nm). This decrease may be attributed to the stabilization of

the system over time or to material degradation in the basic environment.

After annealing in air at  $550 \text{ }^\circ\text{C}$  for 1 h, all coatings generate significantly higher photocurrent densities. After 60 s of testing,  $J_{\text{ph}} \approx 180$ , 200 and  $340 \mu\text{A}/\text{cm}^2$  are obtained for the  $190 \pm 60$ ,  $320 \pm 70$  and  $610 \pm 120$  nm samples, respectively (Fig. 17b). Accordingly, annealing in air can lead to  $J_{\text{ph}}$  values that are 20 or 50 times higher than those of the as-sprayed samples. This beneficial effect is particularly enhanced for the thicker coating ( $610 \pm 120$  nm). However, for all samples, the photocurrent density tends to decrease during testing, at the end of the test reaching minimum values of  $J_{\text{ph}} \approx 100$ , 120 and  $190 \mu\text{A}/\text{cm}^2$  for the  $190 \pm 60$ ,  $320 \pm 70$  and  $610 \pm 120$  nm samples, respectively. Moreover, all the curves exhibit transient current spikes when the illumination is interrupted by chopping the light. This feature is more pronounced for the thicker coating ( $610 \pm 120$  nm), and it increases over time. These spikes may be attributed to surface recombination processes, which further limit the charge carrier generation.

## Discussion

The bonding mechanisms in aerosol deposition are still under discussion (Ref 42). The main models proposed so far are based on room-temperature impact consolidation (Ref 40, 48), stress localization and fragmentation (Ref 43) or deformation (Ref 45, 53). Experimental and simulation results suggest that coating formation is usually associated with particle refinement by fracturing and plastic deformation upon impact (Ref 38, 40, 41, 44, 45, 48). Evidence of plastic deformation for fine ceramic particles has been reported by Akedo et al. (Ref 40), Östlund et al. (Ref 54) and Calviè et al. (Ref 55).

Similarly to cold spray, in the AD process, the spraying parameters should be adjusted to find a window of deposition (Ref 41). First of all, the particle velocity must exceed a critical value to establish proper coating formation. Secondly, the particle size must be in a well-defined range since very small particles are prone to be deflected by bow shock effect, while too coarse particles either fracture (Ref 45) or by too high kinetic energies upon impact lead to abrasive blasting of the substrate (Ref 41). However, estimating critical velocities and suitable size ranges for a given material in AD is still a topic under research. So far, experimentally determined critical velocity is only reported for  $\text{Al}_2\text{O}_3$ ,  $\text{SiO}_2$  and PZT particles (Ref 43, 48, 56) and roughly confirmed by modeling (Ref 45). Nevertheless, reasonable considerations have been made here by referring to the work of Jun Akedo, who demonstrated that the attainable particle velocity generally increases with (1) the

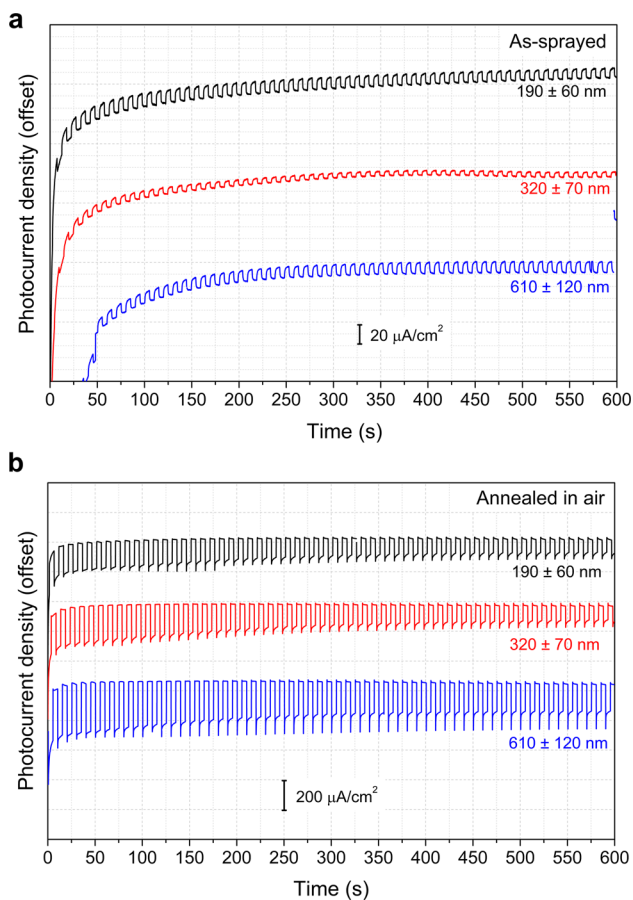


**Fig. 17** Photocurrent densities by chrono-amperometry of  $\text{CuFeO}_2$  thin films in the as-sprayed (a) and air-annealed (b) condition over a testing duration of 600 s at  $+0.44 \text{ V}$  vs RHE in 1 M NaOH solution under chopped illumination are compared. Black, red and blue curves refer to samples with thicknesses of  $190 \pm 60$ ,  $320 \pm 70$  and  $610 \pm 120$  nm, respectively. To avoid curves overlapping, curves were plotted with an offset, and a reference value is given in the graphs

gas flow, thus gas pressure and (2) by using helium as process gas rather than air or nitrogen (Ref 40, 48). Within this chapter, the present understanding should be transferred to aerosol deposition of  $\text{CuFeO}_2$  and respective influences by process gas type and pressure as well as particles sizes on successful coating formation.

### Coating Formation and Adhesion

In the present work, a broadening of the XRD peaks of the coatings in comparison with that of the initial powder is observed for all spraying conditions, indicating grain refinement and induced microstrain (Fig. 4). Although quantitative data on grain refinement were not derived due to the lack of reference data for the synthesized material and the rather complex crystal structure, the general features agree well to previously published results.

The results of the SEM observations show that, for  $\text{CuFeO}_2$ , successful layer formation and full surface coverage can be obtained by using fine particles ( $D_{50} \leq 1 \mu\text{m}$ ), regardless of the gas pressure and type. The coating thickness can be enhanced by increasing the nitrogen gas pressure or by using helium as process gas, while also reducing coating porosity. Coarser particles ( $D_{50} > 1 \mu\text{m}$ ), on the other hand, need specific spraying conditions to form a continuous layer. In case of using nitrogen as process gas, only a gas pressure of  $2.9 \times 10^{-1}$  MPa allows to coat the substrate with a sufficiently regular layer. This is probably related to the need to exceed a critical particle velocity, which depends on particle size. Under the same spraying conditions, smaller particles can reach higher velocities than the coarser ones. Therefore, it can be reasonably inferred here that mild spraying conditions (i.e. using nitrogen at low gas pressure) are only sufficient to accelerate the fine particles ( $D_{50} \leq 1 \mu\text{m}$ ) above the critical velocity and assuring bonding. It should also be noted that, while coarse particles form rather thin layers ( $\leq 1.4 \mu\text{m}$ ) for all spraying conditions, the sub-micrometer powders ( $D_{50} = 0.6 \mu\text{m}$ ) reach coating thickness between 8 and 12  $\mu\text{m}$  depending on the gas pressure. Apart from the ability for bonding, “enhancing” the spraying conditions (i.e., increasing the gas pressure or using helium as process gas) also ensures better coating densification, presumably because it results in the attainment of higher particle velocities. The film growth is thus mainly enhanced by spraying finer particles rather than by increasing the gas pressure, confirming that the particle size plays a major role in the deposition of  $\text{CuFeO}_2$  powders.

More insights on adhesion and deformation were provided by the single-particle impact tests. When particles with a median size of  $2.2 \mu\text{m}$  collide with the substrate surface, multiple craters are formed by unsuccessful impacts. Their numbers and sizes vary with the spraying

conditions. For a “mild” condition (nitrogen as process gas, pressure of  $0.9 \times 10^{-1}$  MPa) most of the impacts result in rebounding, leaving small angular indents on the substrate surface. The rise in gas pressure from  $0.9 \times 10^{-1}$  to  $2.9 \times 10^{-1}$  MPa and the corresponding increase in particle velocity result in more prominent partial penetration of coarse particles into the substrate surface. Further “enhancing” the particle velocities using helium as process gas, results in the increase of successful impacts. The overall number of empty craters decreases, while the number of bonded particles increases. Most of the adhering particle (90%) exhibit a diameter significantly lower than the starting median size, indicating that fracture occurred. On the other hand, only few fragments show signs of internal deformation or flattening. In addition, larger craters are formed on the substrate surface. These features suggest that enhancing the spraying conditions does not necessarily have a beneficial effect on bonding. Higher particles’ velocities result in higher attainable kinetic energies upon impact. However, in this case, when particles are too large ( $D_{50} > 1 \mu\text{m}$ ), they either erode the substrate surface or break due to brittle ceramic behavior, forming small but undeformed fragments. Therefore,  $\text{CuFeO}_2$  particles with a median size of  $2.2 \mu\text{m}$  are too coarse for proper adhesion and coating formation by AD.

Powders with dimension  $\leq 1 \mu\text{m}$  are more suitable for the deposition, as enhanced particles’ adhesion and deformation are observed in the single-impact tests. For this sizes range, further distinctions can be made for the medium ( $D_{50} = 1 \mu\text{m}$ ) and the lower size powders ( $D_{50} = 0.6 \mu\text{m}$ ). By spraying with nitrogen as process gas, signs of rebounding can be observed for the  $D_{50} = 1 \mu\text{m}$  particles, roughly indicating that only 50% of the impacts resulted in successful bonding. However, higher ‘rates’ of successful impacts (> 90%) can be obtained by spraying the finer particles under the same conditions. This difference is probably attributed to the higher velocities that can be attained by the smaller particles. On the other hand, when helium is used as process gas, comparable amounts of successful impacts are obtained for the two sets of powder sizes. Moreover, most of the fragments (80%) that can be observed on the substrate surface exhibit dimensions between 20-40 nm and 600-800 nm and flattened morphologies, indicating that sufficient particle velocities to induce particle fragmentation and deformation were obtained for both sets. However, within the given range of sizes and parameter sets, the small differences in the possibly attainable particle velocities by the two powder sizes do not allow to derive significant influences on coating formation.

In the present case, aerosol deposition of  $\text{CuFeO}_2$  onto heated metal substrates does not offer any benefits for the coating formation. The obtained coatings are rather

inhomogeneous, with less refined microstructures, and contain high amounts of pores and cracks. For increased substrate temperatures, the single-particle impact morphologies indicate, on the one hand, fewer empty craters (i.e., less rebounding), but, on the other hand, also less particle deformation. Thus, it can be concluded that the deformation of the thermally softened steel surfaces results in less particle deceleration. Consequently, the particles might embed more efficiently, but they also show less deformation and fracture. The latter effect, which is detrimental to the quality of the coating, counterbalances and offsets the former. A similar consideration is probably valid for particles that hit already deposited coating layers. This agrees well with the models reported in literature, according to which the bonding mechanism and coating quality depends on both particle deformation and refinement upon impact (Ref 38, 41, 45). Moreover, these results confirm that grain refinement mainly depends on fracture and deformation rather than local heat since even rather long exposure to temperatures of up to 400 °C for several minutes does not induce recrystallization and/or grain refinement. Thus, it can be concluded that local temperature rises during impact possibly support deformation by activating secondary slip systems, but the locally reached temperatures and times for heat exposure are not sufficient to activate recrystallization.

### Parameters Adaptation for Thin Layers

In order to ensure good photoelectrochemical performances, the photoelectrode coatings should be sufficiently dense and well bonded to the substrate surface, with defect-free interfaces. Moreover, the layers should be thinner than 1  $\mu\text{m}$ , the optimum thickness depending on the photoelectrode material (Ref 15). In order to maximize the PEC performance of  $\text{CuFeO}_2$ , effects by coating thickness were separately investigated. The results of this work demonstrate that continuous, rather dense and well-bonded coatings can be obtained by spraying particles with dimension  $\leq 1 \mu\text{m}$  by using either nitrogen at high gas flow/pressure or helium as process gas. Respectively, powders with a median size of 1 and 0.6  $\mu\text{m}$  were selected for the deposition on FTO-glass substrates. With such fine particles, rather thick coatings were build-up (up to 12  $\mu\text{m}$  for one layer), thus needing different strategies to reduce the layer thickness. Decreasing the feeding rate and changing the traverse speeds are the two main strategies used for reducing the coating thickness in kinetic spray methods. Unfortunately, in this case, decreasing the feeding rate by 2 or 4 times only resulted in incomplete or highly discontinuous layer formation. This may indicate that a fraction of the particles with a median size of  $D_{50} = 0.6 \mu\text{m}$  are deflected before reaching the substrate

surface or is removed from the substrate by the subsequent impact of coarser particles or agglomerates. There might also be possible fluctuations in powder feed rates, resulting in local variation in powder deposition. However, since the variation of feed rates and robot kinematics was performed with nitrogen as process gas, it cannot be excluded that, by enhancing the particle velocities by using helium, better results could be obtained.

In contrast to solely adjusting kinematics, the use of cyclones was found to be more effective in reducing the coating thickness. In addition to an overall reduced powder load within the process gas, the cyclones also remove agglomerates and possible retained large particles, generating a more homogeneous aerosol. Under the use of helium as process gas at a pressure of  $2.9 \times 10^{-1}$  MPa, the coating thickness was further reduced by increasing the traverse speed from 5 mm/s to 10, 15, 20 and 25 mm/s. The results demonstrate that coating thickness can be controlled with a sufficient precision by varying the traverse speed. Using helium as process gas at  $2.9 \times 10^{-1}$  MPa thereby enabled to obtain low coating porosities. With both fine powder batches, sufficiently thin films with low porosity, suitable for PEC water splitting, were obtained. However, spraying the finer feedstock powder ( $D_{50} = 0.6 \mu\text{m}$ ) resulted in slightly higher coating thickness and porosity than obtained using the medium size powder ( $D_{50} = 1 \mu\text{m}$ ). This could be attributed to the higher kinetic energies that larger particles ( $D_{50} = 1 \mu\text{m}$ ) can reach upon impact, resulting into enhanced coating consolidation by hammering of subsequent particles. Since the powder batch with a median size of 1  $\mu\text{m}$  formed coatings with slightly more desirable properties, it was selected for the final application by employing helium as process gas.

### Water Splitting Performance

In the photoelectrochemical water splitting process, the photocathode absorbs the sunlight and generates electron/hole pairs, which are involved in the hydrogen evolution reaction (HER) or in the oxygen evolution reaction (OER), respectively. The charge carriers must be efficiently separated to avoid recombination and transported to the respective interface for reaction. Unfortunately,  $\text{CuFeO}_2$  has poor charge separation and transport properties, resulting in limited photoelectrochemical efficiencies (Ref 31, 34, 57).

All the as-sprayed  $\text{CuFeO}_2$  samples can absorb most of the visible light ( $\geq 78\%$ ), regardless of coating thickness. Optical transitions in the reflectance and transmittance spectra indicate the presence of optical bandgaps in the visible range. However, the as-sprayed thin films only generate poor photocurrent densities ( $\leq 10 \mu\text{A}/\text{cm}^2$ ), which

slightly decrease in time, reaching steady values roughly 1.2–1.3 times lower than the initial ones. No clear dependency on the layer thickness was found. These current values are much lower than the ones reported in the literature for bare  $\text{CuFeO}_2$  thin films deposited by conventional deposition methods. Prevôt et al. (Ref 29) observed a steady-state photocurrent density of about  $25 \mu\text{A}/\text{cm}^2$  for non-optimized  $\text{CuFeO}_2$  films deposited by sol–gel, while higher current densities have been reported by Jiang et al. (Ref 58) for spin-coated  $\text{CuFeO}_2$  films ( $\approx 40 \mu\text{A}/\text{cm}^2$ ) and by Read et al. (Ref 30) for electrodeposited  $\text{CuFeO}_2$  electrodes ( $J_{\text{ph}}$  between 85 and  $160 \mu\text{A}/\text{cm}^2$ ). The discrepancy between the high % of absorbed light and the low photoelectrochemical performance of AD coatings may indicate high ohmic losses during charge separation and diffusion.

After annealing in air, the coatings generate significantly higher photocurrent densities (from 180 to  $340 \mu\text{A}/\text{cm}^2$  according to coating thickness), outperforming bare  $\text{CuFeO}_2$  thin films deposited by sol–gel, spin coating and electrodeposition methods (Ref 29, 30, 58). Better performances for  $\text{CuFeO}_2$  coatings, up to  $J_{\text{ph}} \approx 2.4 \text{ mA}/\text{cm}^2$ , have only been reported in the literature for optimized photoelectrodes, by means of post-deposition hybrid microwave annealing (Ref 32) and/or using catalyst and protective overlayers (Ref 29, 32) or heterojunctions (Ref 33). More reference data can be found in Table S1 of (Ref 32). In this work, the increase in the photocurrent density is more pronounced for the thicker coating ( $620 \pm 120 \text{ nm}$ ), which exhibit 50 times higher values after annealing. This is obtained despite a slightly reduced ability of the coatings to absorb the visible after annealing in air, such being more pronounced for the thinner coating ( $190 \pm 60 \text{ nm}$ ).

In summary, annealing in air is highly efficient to reduce the ohmic losses given in the as-deposited samples. Charge carriers' recombination in the as-sprayed samples can possibly be attributed to effective diffusion pathways and active recombination centers, then both being reduced by annealing. The effective diffusion pathways can be reduced by closing non-bonded interfaces within the coating and to the substrate, as well as by decreasing the porosities of the as-sprayed coatings. In addition, amounts of possibly active centers for recombination given by local crystal defects and internal stresses could be reduced by annealing. Apart from that, the better PEC performance after annealing might be also attributed to the oxygen intercalation into the delafossite structure. As demonstrated by Jang et al. (Ref 32), thermal treatments in air can cause doping of the  $\text{CuFeO}_2$  lattice, resulting in increased charge conductivity, thus allowing for more efficient charge separation. In summary, a combination of all above phenomena contributes to the enhanced photocurrent densities after annealing of as deposited thin  $\text{CuFeO}_2$  films, within the present study so far not allowing for distinction of

individual influences, but further investigations are currently under investigation.

The results of this work are rather promising, demonstrating the feasibility of using AD and well-tuned post-deposition annealing for processing highly effective photocathodes for sunlight harvesting. However, for practical applications, the aerosol-deposited  $\text{CuFeO}_2$  films must be further optimized to achieve high chemical stability and performances over long periods of time. Faster reaction kinetics and more efficient charge carrier separation (i.e., better PEC performances) can be obtained by decorating the thin films surfaces with catalyst nanoparticles, while protective overlayers can prevent material degradation under operating conditions.

## Summary and Conclusions

$\text{CuFeO}_2$  powders were synthesized through a solid-state synthesis technique and deposited by AD on stainless steel and FTO-glass substrates. In the first part of this work, the effects of (i) powder size, (ii) process gas, (iii) gas flow/pressure and (iv) substrate temperature were explored by spraying onto AISI 304 steel substrates. The best spraying parameters were then tuned to deposit thin films on FTO-glass substrates for the final application. The study allows to draw the following conclusions for aerosol deposition of  $\text{CuFeO}_2$ :

- Feedstock powders with a median size ( $D_{50}$ )  $\leq 1 \mu\text{m}$  are more suitable for aerosol deposition, leading to the formation of more continuous and less porous layers. This is attributed to the high attainable particle velocities, which result in enhanced particle deformation and associated fragmentation and consolidation upon impact. High gas pressure allows to deposit also more of the coarser particles, but single-impact tests reveal that insufficient particle deformation is obtained under such spraying conditions.
- For fine powders ( $\leq 1 \mu\text{m}$ ), higher gas pressure results in enhanced particle deformation and fragmentation upon impact, leading to less porous coatings. This effect is more prominent for using helium as process gas.
- In the present case of aerosol deposition of  $\text{CuFeO}_2$  on AISI 304 steel plates, substrate heating has no beneficial effect on coating formation, here possibly given by reduced particle deformation and fragmentation.
- Thin films ( $< 1 \mu\text{m}$ ) can be obtained by employing cyclones to cut off agglomerates and coarser particles and guaranteeing a more continuous powder load with the gas stream in combination with increased traverse in line robot velocities. When helium is employed as

process gas, coating thickness can be easily adjusted by traverse speed variation. Spraying particles with a median size of 1  $\mu\text{m}$  leads to slightly thinner and less porous coatings as compared to using a finer powder (median size of 0.6  $\mu\text{m}$ ).

Optical properties and photoelectrochemical performances of three sets of coatings with different thickness values were investigated in as-sprayed state and after a thermal treatment in air. The results clearly show that annealing in air increases the photoelectrochemical efficiency. In particular, the current density can be maximized by using films with an average thickness of 620 nm annealed in air for 1 h at 550  $^{\circ}\text{C}$ , reaching a current density of 340  $\mu\text{A}/\text{cm}^2$ , comparable to or slightly higher than photocurrent densities reported in the literature for layers processed by sol–gel, spin coating or electrochemical methods.

In summary, aerosol deposition proves to be a suitable first step within the process chain to produce  $\text{CuFeO}_2$  photocathode coatings in sufficient quality for possible applications. Photoelectrochemical efficiency comparable to state-of-the-art coatings can be obtained by optimizing the coating thickness and by annealing, while taking advantage of the high deposition rate and cost-effectiveness of the AD method. However, there is still space for further material optimization by means of depositing protective or catalyst overlayers to assure higher efficiencies and stability over time.

**Acknowledgments** The authors greatly acknowledge the financial support over the Erasmus exchange program. All authors thank Dr. Jiri Kollmann from Hereon and Dr. Magdalena Gualtieri from UNIMORE for technical support and fruitful discussions.

**Funding** Open access funding provided by Università degli Studi di Modena e Reggio Emilia within the CRUI-CARE Agreement.

**Open Access** This article is licensed under a Creative Commons Attribution 4.0 International License, which permits use, sharing, adaptation, distribution and reproduction in any medium or format, as long as you give appropriate credit to the original author(s) and the source, provide a link to the Creative Commons licence, and indicate if changes were made. The images or other third party material in this article are included in the article's Creative Commons licence, unless indicated otherwise in a credit line to the material. If material is not included in the article's Creative Commons licence and your intended use is not permitted by statutory regulation or exceeds the permitted use, you will need to obtain permission directly from the copyright holder. To view a copy of this licence, visit <http://creativecommons.org/licenses/by/4.0/>.

## References

1. A. Nemmour, A. Inayat, I. Janajreh, and, C. Ghenai, Green Hydrogen-Based E-Fuels (E-Methane, E-Methanol, E-Ammonia) to Support Clean Energy Transition: A Literature Review, *Int. J. Hydrogen Energy*, 2023, **48**(75), p 29011-29033. <https://doi.org/10.1016/j.ijhydene.2023.03.240>
2. R. Daiyan, I. Macgill, and R. Amal, Opportunities and Challenges for Renewable Power-to-X, *ACS Energy Lett.*, 2020, **5**(12), p 3843-3847.
3. W. Liu, H. Zuo, J. Wang, Q. Xue, B. Ren, and F. Yang, The Production and Application of Hydrogen in Steel Industry, *Int. J. Hydrogen Energy*, 2021, **46**(17), p 10548-10569. <https://doi.org/10.1016/j.ijhydene.2020.12.123>
4. J. Töppler and J. Lehmann, *Hydrogen and Fuel: Technologies and Market Perspectives*, Springer, USA, 2016.
5. M.R. Usman, Hydrogen Storage Methods: Review and Current Status, *Renew. Sustain. Energy Rev.*, 2022, **167**(20), p 112743. <https://doi.org/10.1016/j.rser.2022.112743>
6. M. Klell, Chapter 1: Storage of Hydrogen in the Pure Form, *Handbook of Hydrogen Storage: New Materials for Future Energy Storage*, 2010, p 1-37. <https://doi.org/10.1002/9783527629800>
7. J. Huot, Chapter 4: Metal Hydrides, *Handbook of Hydrogen Storage: New Materials for Future Energy Storage*, 2007, p 81-166. <https://doi.org/10.1002/9783527629800>
8. C.M. Kalamaras and A.M. Efstathiou, Hydrogen Production Technologies: Current State and Future Developments, *Conf. Pap. Energy*, 2013, **2013**, p 1-9.
9. I. Dincer and C. Acar, Review and Evaluation of Hydrogen Production Methods for Better Sustainability, *Int. J. Hydrogen Energy*, 2014, **40**(34), p 11094-11111. <https://doi.org/10.1016/j.ijhydene.2014.12.035>
10. F. Suleman, I. Dincer, and M. Agelin-Chaab, Environmental Impact Assessment and Comparison of Some Hydrogen Production Options, *Int. J. Hydrogen Energy*, 2015, **40**(21), p 6976-6987. <https://doi.org/10.1016/j.ijhydene.2015.03.123>
11. M. Hermesmann and T.E. Müller, Green, Turquoise, Blue, or Grey? Environmentally Friendly Hydrogen Production in Transforming Energy Systems, *Prog. Energy Combust. Sci.*, 2022, **90**(October 2021), p 100996. <https://doi.org/10.1016/j.peccs.2022.100996>
12. C. Ros, T. Andreu, and J.R. Morante, Photoelectrochemical Water Splitting: A Road from Stable Metal Oxides to Protected Thin Film Solar Cells, *J. Mater. Chem. A*, 2020, **8**(21), p 10625-10669.
13. P. Chatterjee, M.S.K. Ambati, A.K. Chakraborty, S. Chakraborty, S. Biring, S. Ramakrishna, T.K.S. Wong, A. Kumar, R. Lawaniya, and G.K. Dalapati, Photovoltaic/Photo-Electrocatalysis Integration for Green Hydrogen: A Review, *Energy Convers. Manag.*, 2022, **261**(April), p 115648. <https://doi.org/10.1016/j.enconman.2022.115648>
14. K. Sivula and M.S. Prevo, Photoelectrochemical Tandem Cells for Solar Water Splitting, *J. Phys. Chem. C*, 2013, **117**, p 17879-17893.
15. Z. Chen, H.N. Dinh, and E. Miller, *Photoelectrochemical Water Splitting: Standards, Experimental Methods, and Protocols*, Springer, New York, 2013. <https://doi.org/10.1007/978-1-4614-8298-7>
16. M. Mohsin, T. Ishaq, I.A. Bhatti, A. Jilani, A.A. Melaibari, and N.H. Abu-Hamdeh, Semiconductor Nanomaterial Photocatalysts for Water-Splitting Hydrogen Production: The Holy Grail of Converting Solar Energy to Fuel, *Nanomater.*, 2023, **13**(3), p 546.
17. Z. Li, W. Luo, M. Zhang, J. Feng, and Z. Zou, Photoelectrochemical Cells for Solar Hydrogen Production: Current State of

- Promising Photoelectrodes, Methods to Improve Their Properties, and Outlook, *Energy Environ. Sci.*, 2013, **6**(2), p 347-370.
18. X. van de Krol and M. Grätzel, Photoelectrochemical Hydrogen Production. Roel van de Krol and Michael Grätzel, Eds., Springer, 2012. <https://doi.org/10.1007/978-1-4614-1380-6>
  19. I.R. Hamdani and A.N. Bhaskarwar, Recent Progress in Material Selection and Device Designs for Photoelectrochemical Water-Splitting, *Renew. Sustain. Energy Rev.*, 2021, **138**(October 2020), p 110503. <https://doi.org/10.1016/j.rser.2020.110503>
  20. J. Tang, J.R. Durrant, and D.R. Klug, Mechanism of Photocatalytic Water Splitting in TiO<sub>2</sub>. Reaction of Water with Photoholes, Importance of Charge Carrier Dynamics, and Evidence for Four-Hole Chemistry, *J. Am. Chem. Soc.*, 2008, **130**(42), p 13885-13891.
  21. X. Zhang, S. Zhang, X. Cui, W. Zhou, W. Cao, D. Cheng, and Y. Sun, Recent Advances in TiO<sub>2</sub>-Based Photoanodes for Photoelectrochemical Water Splitting, *Chem. Asian J.*, 2022, **17**(20), p e202200668.
  22. M. Tayebi and B.K. Lee, Recent Advances in BiVO<sub>4</sub> Semiconductor Materials for Hydrogen Production Using Photoelectrochemical Water Splitting, *Renew. Sustain. Energy Rev.*, 2019, **111**(January), p 332-343. <https://doi.org/10.1016/j.rser.2019.05.030>
  23. J.H. Kim and J.S. Lee, Elaborately Modified BiVO<sub>4</sub> Photoanodes for Solar Water Splitting, *Adv. Mater.*, 2019, **31**(20), p 1-35.
  24. A. Elsenberg, T. Emmmler, M. Schieda, F. Gärtner, and T. Klassen, Tuning Aerosol Deposition of BiVO<sub>4</sub> Films for Effective Sunlight Harvesting, *J. Therm. Spray Technol.*, 2023, **32**, p 352-362.
  25. K. Sivula, F. Le Formal, and M. Grätzel, Solar Water Splitting: Progress Using Hematite ( $\alpha$ -Fe<sub>2</sub>O<sub>3</sub>) Photoelectrodes, *ChemSuschem*, 2011, **4**(4), p 432-449.
  26. C. Li, J. He, Y. Xiao, Y. Li, and J.J. Delaunay, Earth-Abundant Cu-Based Metal Oxide Photocathodes for Photoelectrochemical Water Splitting, *Energy Environ. Sci.*, 2020, **13**(10), p 3269-3306.
  27. R. Siavash Moakhar, S.M. Hosseini-Hosseinabad, S. Masudypanah, A. Seza, M. Jalali, H. Fallah-Arani, F. Dabir, S. Gholipour, Y. Abdi, M. Bagheri-Hariri, N. Riahi-Noori, Y.F. Lim, A. Hagfeldt, and M. Saliba, Photoelectrochemical Water-Splitting Using CuO-Based Electrodes for Hydrogen Production: A Review, *Adv. Mater.*, 2021 <https://doi.org/10.1002/adma.202007285>
  28. F.F. Abdi and S.P. Berglund, Recent Developments in Complex Metal Oxide Photoelectrodes, *J. Phys. D: Appl. Phys.*, 2017, **50**(19), p 193002.
  29. M.S. Prévot, N. Guijarro, and K. Sivula, Enhancing the Performance of a Robust Sol-gel-Processed p-Type Delafossite CuFeO<sub>2</sub> Photocathode for Solar Water Reduction, *ChemSuschem*, 2015, **8**(8), p 1359-1367.
  30. C.G. Read, Y. Park, and K.S. Choi, Electrochemical Synthesis of P-Type CuFeO<sub>2</sub> Electrodes for Use in a Photoelectrochemical Cell, *J. Phys. Chem. Lett.*, 2012, **3**(14), p 1872-1876.
  31. M.S. Prévot, X.A. Jeanbourquin, W.S. Bourée, F. Abdi, D. Friedrich, R. Van De Krol, N. Guijarro, F. Le Formal, and K. Sivula, Evaluating Charge Carrier Transport and Surface States in CuFeO<sub>2</sub> Photocathodes, *Chem. Mater.*, 2017, **29**(11), p 4952-4962.
  32. Y.J. Jang, Y. Bin Park, H.E. Kim, Y.H. Choi, S.H. Choi, and J.S. Lee, Oxygen-Intercalated CuFeO<sub>2</sub> Photocathode Fabricated by Hybrid Microwave Annealing for Efficient Solar Hydrogen Production, *Chem. Mater.*, 2016, **28**(17), p 6054-6061.
  33. M.S. Prévot, Y. Li, N. Guijarro, and K. Sivula, Improving Charge Collection with Delafossite Photocathodes: A Host-Guest CuAlO<sub>2</sub>/CuFeO<sub>2</sub> Approach, *J. Mater. Chem. A*, 2016, **4**(8), p 3018-3026.
  34. C.M. Jiang, S.E. Reyes-Lillo, Y. Liang, Y.S. Liu, G. Liu, F.M. Toma, D. Prendergast, I.D. Sharp, and J.K. Cooper, Electronic Structure and Performance Bottlenecks of CuFeO<sub>2</sub> Photocathodes, *Chem. Mater.*, 2019, **31**(7), p 2524-2534.
  35. M. Ferri, J.D. Elliott, M.F. Camellone, S. Fabris, and S. Piccinin, CuFeO<sub>2</sub>-Water Interface under Illumination: Structural Electronic, and Catalytic Implications for the Hydrogen Evolution Reaction, *ACS Catal.*, 2021, **11**(4), p 1897-1910.
  36. C. Wolpert, T. Emmmler, M. Villa Vidaller, A. Elsenberg, K. Shinoda, M. Schieda, F. Gärtner, J. Akedo, and T. Klassen, Aerosol-Deposited BiVO<sub>4</sub> Photoelectrodes for Hydrogen Generation, *J. Therm. Spray Technol.*, 2020, **30**, p 603-616.
  37. J. Akedo, S. Nakano, J. Park, S. Baba, and K. Ashida, The Aerosol Deposition Method, *Synthesiology*, 2008, **1**(2), p 121-130.
  38. J. Akedo, Room Temperature Impact Consolidation and Application to Ceramic Coatings: Aerosol Deposition Method, *J. Ceram. Soc. Jpn.*, 2020, **128**(3), p 101-116.
  39. J. Akedo and M. Lebedev, Microstructure and Electrical Properties of Lead Zirconate Titanate (Pb(Zr<sub>52</sub>/Ti<sub>48</sub>)O<sub>3</sub>) Thick Films Deposited by Aerosol Deposition Method, *Jpn. J. Appl. Phys. Part 1*, 1999, **38**(9B), p 5397-5401.
  40. J. Akedo, Room Temperature Impact Consolidation (RTIC) of Fine Ceramic Powder by Aerosol Deposition Method and Applications to Microdevices, *J. Therm. Spray Technol.*, 2008, **17**(2), p 181-198.
  41. D. Hanft, J. Exner, M. Schubert, T. Stöcker, P. Fuierer, and R. Moos, An Overview of the Aerosol Deposition Method: Process Fundamentals and New Trends in Materials Applications, *J. Ceram. Sci. Technol.*, 2015, **6**(3), p 147-181.
  42. K. Shinoda, F. Gaertner, C. Lee, A. Dolatabadi, and S. Johnson, Kinetic Spraying of Brittle Materials: From Layer Formation to Applications in Aerosol Deposition and Cold Gas Spraying, *J. Therm. Spray Technol.*, 2021, **30**, p 471-479.
  43. H. Kwon, Y. Kim, H. Park, and C. Lee, Impact Behavior for Successful Particle-Particle Bonding in Vacuum Kinetic Spraying, *J. Therm. Spray Technol.*, 2021, **30**(3), p 542-557. <https://doi.org/10.1007/s11666-020-01078-7>
  44. J. Exner, M. Schubert, D. Hanft, J. Kita, and R. Moos, How to Treat Powders for the Room Temperature Aerosol Deposition Method to Avoid Porous, Low Strength Ceramic Films, *J. Eur. Ceram. Soc.*, 2019, **39**(2-3), p 592-600. <https://doi.org/10.1016/j.jeurceramsoc.2018.08.008>
  45. B. Daneshian, F. Gärtner, H. Assadi, M.V. Vidaller, D. Höche, and T. Klassen, Features of Ceramic Nanoparticle Deformation in Aerosol Deposition Explored by Molecular Dynamics Simulation, *Surf. Coat. Technol.*, 2021, **2022**, p 429.
  46. T. Stöcker, J. Exner, M. Schubert, M. Streibl, and R. Moos, Influence of Oxygen Partial Pressure during Processing on the Thermoelectric Properties of Aerosol-Deposited CuFeO<sub>2</sub>, *Materials*, 2016, **9**(4), p 1-16.
  47. T.R. Zhao, M. Hasegawa, and H. Takei, Crystal Growth and Characterization of Cuprous Ferrite (CuFeO<sub>2</sub>), *J. Cryst. Growth*, 1996, **166**(1-4), p 408-413.
  48. J. Akedo, Aerosol Deposition of Ceramic Thick Films at Room Temperature: Densification Mechanism of Ceramic Layers, *J. Am. Ceram. Soc.*, 2006, **89**(6), p 1834-1839.
  49. W.K. Tan, Y. Shigeta, A. Yokoi, G. Kawamura, A. Matsuda, and H. Muto, Investigation of the Anchor Layer Formation on Different Substrates and Its Feasibility for Optical Properties Control by Aerosol Deposition, *Appl. Surf. Sci.*, 2019, **483**(November 2018), p 212-218. <https://doi.org/10.1016/j.apsusc.2019.03.278>
  50. N. Ziani, E. Aubry, N. Martin, L. Hirsinger, A. Billard, P. Briois, M.S. Belkaid, and M. Arab Pour Yazdi, Influence of Substrate Temperature on Delafossite CuFeO<sub>2</sub> Films Synthesized by Reactive Magnetron Sputtering, *J. Alloys Compd.*, 2021, **876**, p 160169. <https://doi.org/10.1016/j.jallcom.2021.160169>

51. Z. Deng, X. Fang, S. Wu, S. Wang, W. Dong, J. Shao, and R. Tao, The Effect of Oxygen Partial Pressure on the Properties of CuFeO<sub>2</sub> Thin Films Prepared by RF Sputtering, *Vacuum*, 2015, **115**, p 1-5. <https://doi.org/10.1016/j.vacuum.2015.01.025>
52. H.Y. Chen and G.W. Fu, Influences of Post-Annealing Conditions on the Formation of Delafossite-CuFeO<sub>2</sub> Thin Films, *Appl. Surf. Sci.*, 2014, **288**, p 258-264. <https://doi.org/10.1016/j.apsusc.2013.10.017>
53. B. Daneshian, F. Gaertner, H. Assadi, D. Hoeche, W. Weber, and T. Klassen, Size Effects of Brittle Particles in Aerosol Deposition—Molecular Dynamics Simulation, *J. Therm. Spray Technol.*, 2021, **30**(3), p 503-522. <https://doi.org/10.1007/s11666-020-01149-9>
54. F. Östlund, K. Rzepiejewska-Malyska, K. Leifer, L.M. Hale, Y. Tang, R. Ballarini, W.W. Gerberich, and J. Michler, Brittle-to-Ductile Transition in Uniaxial Compression of Silicon Pillars at Room Temperature, *Adv. Funct. Mater.*, 2009, **19**(15), p 2439-2444.
55. E. Calvié, J. Réthoré, L. Joly-Pottuz, S. Meille, J. Chevalier, V. Garnier, Y. Jorand, C. Esnouf, T. Epicier, J.B. Quirk, and K. Masenelli-Varlot, Mechanical Behavior Law of Ceramic Nanoparticles from Transmission Electron Microscopy in Situ Nano-Compression Tests, *Mater. Lett.*, 2014, **119**, p 107-110. <https://doi.org/10.1016/j.matlet.2014.01.002>
56. Y. Furuya, S. Konuma, and M. Hasegawa, Deposition Mechanism of Alumina Particles in Aerosol Deposition Based on the Kinetic Energy of Particles, *Surf. Coat. Technol.*, 2023, **458**(February), p 129362. <https://doi.org/10.1016/j.surfcoat.2023.129362>
57. Y. Hermans, A. Klein, H.P. Sarker, M.N. Huda, H. Junge, T. Toupance, and W. Jaegermann, Pinning of the Fermi Level in CuFeO<sub>2</sub> by Polaron Formation Limiting the Photovoltage for Photochemical Water Splitting, *Adv. Funct. Mater.*, 2020 <https://doi.org/10.1002/adfm.201910432>
58. T. Jiang, Y. Zhao, and H. Xue, Boosting the Performance of Delafossite Photocathode Through Constructing a CuFeO<sub>2</sub>/CuO Heterojunction for Photoelectrochemical Water Reduction, *J. Mater. Sci.*, 2019, **54**(18), p 11951-11958. <https://doi.org/10.1007/s10853-019-03747-7>

**Publisher's Note** Springer Nature remains neutral with regard to jurisdictional claims in published maps and institutional affiliations.